Structures 65 (2024) 106668

Contents lists available at ScienceDirect

Structures

journal homepage: www.elsevier.com/locate/structures

Finite element modeling of composite plate shear walls/concrete-filled (C-PSW/CF)

Emre Kizilarslan [a,*,1], Hadi Kenarangi [b,2], Michel Bruneau [a,3]

[a] Dept. of Civil Structural and Environmental Engineering, Univ. at Buffalo, Buffalo, NY 14260, United States
[b] Dynamics Engineer, SpaceX, Hawthorne, CA, United States

ARTICLE INFO

Keywords:
Composite plate shear walls
Finite Element Modeling
Steel Fracture
Composite Behavior
Hysteretic behavior
Contact surface model

ABSTRACT

A Composite Plate Shear Wall/Concrete Filled (C-PSW/CF) is a "sandwich" type of construction by which concrete (without rebars) is enclosed between steel plates connected by tie bars. Since this system is relatively new, researchers as well as practicing engineers sometimes need to develop nonlinear model of these walls to be able to run pushover analyses, cyclic analyses, and seismic response analysis of C-PSW/CF. Different methods can be used for such non-linear analysis, as a function of project needs and computational resolution desired. This paper focuses on finite element modelling; it describes the details of the LS-DYNA models of the C- and T- shaped C-PSW/CF specimens tested in SEESL at University at Buffalo and shows the comparison between test data with the results of finite element analysis of specimens. As such, the objective of this paper is to present the details of a model used to replicate the hysteretic behavior of the tested specimens, and then answers questions that cannot be investigated or measured from tested specimens. More specifically, this allowed to quantify the respective contributions of steel and concrete to the total flexural strength throughout the entire cyclic history, where (for example) steel contributed to 54 % of the total flexural strength in the positive direction during the initial cycles of hysteretic response, degrading to 45 % at the onset of local buckling in the web, but recovering to 80 % upon strength global strength degradation of the wall.

1. Introduction

A Composite Plate Shear Wall/Concrete Filled (C-PSW/CF), a.k.a SpeedCore walls, is a relatively new type of walls for which concrete (without rebars) is enclosed between steel plates that are connected by tie bars. A number of different types of composite walls have been investigated by other researchers, although most differ in fundamental ways from C-PSW/CF. The most commonly studied of these alternate systems has been composite steel-concrete shear walls with vertical steel profiles encased in reinforced concrete; for example, Dan et al. [1] and Rahai and Hatami [2] performed experimental and numerical studies on such walls of different configurations and having different shear studs spacing. Another type of composite shear wall investigated by Zhao and Astaneh-Asl [3–5] consisted of adding reinforced concrete panels to sandwich the plates of a conventional Steel Plate Shear Wall (SPSW, of the type described in AISC 341). These panels were added on one side or both sides of the steel plate and served to prevent its buckling during cyclic inelastic response. A gap was left between the panels and the beams and columns of the SPSW to prevent them from developing a diagonal compressive strut that would contribute to lateral load resistance (at least until drift are large enough to close the gap [6]). Along similar lines, Rahnavard et al. [6] performed numerical studies of such walls, with and without gaps and with concrete cast on one or both sides of the steel plate. They investigated the effect of various parameters (such as distance between connectors, concrete thickness, concrete tensile strength) on hysteresis response, out of plane displacement, drift, and dissipated energy. Yet, SPSW surrounded by reinforced concrete panels, and reinforced concrete walls with encased steel shapes, differ in many significant ways from C-PSW/CF, both in configuration and ultimate behavior.

A number of studies have investigated the behavior of C-PSW/CF of the type considered here, but subjected to monotonic loading. A basic

* Corresponding author.
E-mail addresses: emrekizi@buffalo.edu (E. Kizilarslan), hadikena@buffalo.edu (H. Kenarangi), bruneau@buffalo.edu (M. Bruneau).
[1] ORCID: https://orcid.org/0000–0003-3014–1165
[2] https://orcid.org/0000–0002-8750–7722
[3] http://orcid.org/0000–0003-1170–468X

https://doi.org/10.1016/j.istruc.2024.106668
Received 20 October 2022; Received in revised form 7 May 2024; Accepted 27 May 2024
Available online 19 June 2024

design methodology for double skin composite elements subjected to axial and bending loads has been defined by Wright et al. [7]. McKinley and Baswell [8] developed an analytical solution for the elastic-plastic behavior of Bi-Steel panels or double skin composite panels (which are essentially C-PSW/CF of a different name) and commented on their ability to develop large deformations before failure. Wright and Gallocher [9] investigated the ultimate capacity of composite walls and their benefits over traditional concepts. Omer et al. [10] carried out numerical modeling and analysis of double skin composite plates. It was found that concrete core failure in some cases can be reduced by increasing the size of the side steel plate thickness.

Fewer studies have investigated the cyclic inelastic response of C-PSW/CF. Since this system is fairly new, some researchers and practicing engineers may wish to develop nonlinear models of these walls to perform pushover analyses, cyclic analyses, and seismic response analyses of C-PSW/CF. There might be different ways to build models for such non-linear analyses, based on project needs and computational resolution desired, and having detailed information on finite element models that were successful in replicating global flexural behavior may be of benefit in that perspective. Kizilarslan et al. [11] proposed two different approaches to model these types of walls in the OpenSees program to perform fast 2D nonlinear time history analyses for a FEMA P695 study of Coupled Composite Plate Shear Walls/Concrete-Filled (CC-PSW/CF). In the first approach, walls were modelled using fiber-hinge elements (i.e., distributed plasticity model) modeled with constitutive equations that account for both buckling and fracture of the steel. In the second approach, the walls were modelled with fiber-hinge elements having effective stress-strain curves derived from results of 3D finite element analyses of planar C-PSW/CF using the Abaqus program [12]. In the 2D modelling approach, tie bars were not modeled explicitly. Their effect (i.e., unsupported length of steel plates) was only considered in the buckling parameter of steel material model.

For more detailed information on the behavior of C-SPW/CF, 3D finite element models are necessary. Polat and Bruneau [13 and 14] constructed 3D models using the LS-DYNA program in order to investigate the behavior of different rectangular cross-sections of C-PSW/CF. However, these models were only calibrated with planar walls; also, they did not account for the presence of axial (gravity) loading. More recent modeling by Shafaei et al. [12] included axial loading but was also only calibrated with planar walls. As such, all finite element studies focusing on modeling the cyclic inelastic behavior of such walls have solely focused on the behavior of planar walls. Considering the cross-section shape of C- and T- shaped walls, reversal of neutral axis is significant in different lateral loading directions. A 3D model verification for C- and T- shaped walls under both axial and lateral loading together was needed.

Moreover, during tests of composite walls, it was observed that the strength of walls remained constant during development of local buckling and did not start to drop until the progressive development of fracture, regardless of direction of loading. The FEA models presented here helped to investigate the progressive transfer of load between concrete and steel from initiation of local buckling until fracture. Also, the models developed here also made it possible to conduct (for the first time) a preliminary study of the cumulative plastic strains at fracture for C- and T-shaped walls.

This paper focuses on finite element modelling; it describes the details of the LS-DYNA models of the C- and T-shaped C-PSW/CF specimens tested by Kenarangi et al. [13], and Kizilarslan and Bruneau [14] and shows the comparison between test data with the results of finite element analysis. The objectives of the paper are: (1) to present complete information on the modeling details that must be addressed to provide a satisfactory agreement between numerical and experimental results, more specifically focusing on C- and T-shaped walls as none of the previous modelling studies have provided a verified model demonstrated to be equally applicable to these more complex cross-section shapes (previous studies only focused on planar walls), and; (2) building on the confidence established in the models' ability to replicate global hysteretic behavior, to use this model to better understand the post-buckling the respective contributions of steel and concrete to the total flexural strength of these walls up to fracture (which provides additional information that could not be measured during the tests of the specimens).

Moment versus drift plots are used for this purpose, and the initial stiffness, drifts at which buckling occurred at webs and flanges, maximum strengths in both directions, fracture initiation and progression, and strength deterioration after peaks are compared. The information presented here is expected to be valuable to future researchers who would like to replicate the models and perform parametric studies for these types of walls.

2. Properties of tested specimens

Table 1 summarizes many relevant dimensions and properties for the two C-shapes and four T-shaped specimens, namely: overall dimensions; tie bar spacing and diameter; wall aspect ratios; steel, concrete, and gross areas; reinforcement ratios; yield strength and concrete compressive strength, and target axial loads.

Table 1
Properties of the C- and T-shape Specimens (1 in. = 25.4 mm; 1 ksi = 6.89 MPa; 1 kip = 4.45 kN).

Wall Parameters	Units	Prototype	C1	C2	T1	T2	T3	T4
Wall Height, H	in.	N/A	166	166	166	166	166	166
Flange length, h	in.	360.0	97.5	97.5	48.375	48.375	48.375	48.375
Web length, b	in.	120.0	30.0	30.0	30.0	30.0	30.0	30.0
Steel plate thickness, t_s	in.	1/2	3/16	3/16	3/16	3/16	3/16	3/16
Flange thickness, d	in.	25.0	6.0	6.0	6.0	6.0	6.0	6.0
Web thickness, c	in.	25.0	8.375	8.375	8.375	8.375	8.375	8.375
Tie bar spacing (vertical and horizontal)	In.	12	6	6	6	6	4.5	4.5
Tie bar diameter	In.	1	1/2	1/2	1/2	1/2	1/2	1/4
Wall aspect ratio (height to web), H/b	N/A	N/A	5.53	5.53	5.53	5.53	5.53	5.53
Cross-section aspect ratio, γ=b/h	N/A	0.33	0.31 (=γ_p)	0.31 (=γ_p)	0.62 (=γ_p)	0.62 (=γ_p)	0.62 (=γ_p)	0.62 (=γ_p)
Flange aspect ratio, α=d/h	N/A	0.07	0.06 (=α_p)	0.06 (=α_p)	0.12 (=α_p)	0.12 (=α_p)	0.12 (=α_p)	0.12 (=α_p)
Web aspect ratio, β=c/b	N/A	0.21	0.28 (=t_w)	0.28 (=t_w)	0.28 (=t_w)	0.28 (=t_w)	0.28 (=t_w)	0.28 (=t_w)
Steel area, A_s	$in.^2$	622	61.8	61.8	32.9	32.9	32.9	32.9
Concrete area, A_c	$in.^2$	13128	925.2	925.2	458.4	458.4	458.4	458.4
Gross area, A_g	$in.^2$	13750	987	987	491.25	491.25	491.25	491.25
Reinforcement ratio of web, ρ_{web}	%	4.2	4.5	4.5	2.14	2.14	2.14	2.14
Reinforcement ratio of flange, ρ_{flange}	%	4.2	6.3	6.3	4.6	4.6	4.6	4.6
Reinforcement ratio, ρ_s	%	4.5	6.3	6.3	6.7	6.7	6.7	6.7
Yield strength, F_y	ksi	50	55.4	55.4	54	54	61.07	60.03
Concrete strength, f'_c	ksi	6	4.5	5.1	3.6	5.7	6.03	4.17
Crushing load of concrete, $A_c f'_c$	kips	78770	4163	4719	1650	2613	2662	2049
Target axial load ratio	%	N/A	22	15	247.5	784	799	615

3. Finite element modeling of specimens

The finite element models of the tested specimens were built in LS-DYNA [15]. Figs. 1 and 2 show the individual parts of the FEM models that were assembled to create the complete C- and T-shaped C-PSW/CF specimens, respectively. For simplicity and efficiency, only half of the specimens were modelled with symmetric boundary conditions. The models were also constructed as an assembly of four different systems, namely (for each wall modeled): 1) The wall specimen itself; 2) The axial loading setup (ALS); 3) The lateral loading setup (LLS), and; 4) The reinforced concrete footing. Note that simpler models were tried, but these models could not reach the desired level of accuracy in replicating the test data. By including the axial loading test setup and components of reinforced concrete footing in the FEA model, significantly more accuracy was achieved with the results. This is because, first, no corrections were needed to model the fact that axial load was applied on the specimens by vertically inclined actuators and that these angles changed as the specimen displaced laterally (here, the model accounted directly for the change in angle of actuators during the test). Second, because of the shape of the walls, the contribution of the footing to the overall rotation at the base of the wall due to flexural response was different in the two different loading directions (web in compression or flange in compression). More accurate results were obtained by modeling the concrete footing as well instead of using a spring of constant stiffness (whose single elastic stiffness would have been determined by trial and error) to provide an imperfect footing's rotational spring.

3.1. Modelling of wall specimens

The models of the wall specimens (Fig. 3) consist of steel plates, thicker plates or doubler plates that had been added to the wall specimens at their base (where the wall was embedded into the concrete footing), stiffeners, infill concrete, tie bars (and studs for Specimens T3 and T4), and base plates.

Steel plates, thicker plates (or doubler plates), and stiffeners were modeled using fully integrated quadratic shell elements with Belytschko-Tsay shell formulation (*Shell_16* in LS-DYNA) and three integration points were used through thickness of the elements. The size of the elements were 1*in.* (25.4 *mm*) wide by 1*in.* (25.4 *mm*) in height (except for Specimens T3 and T4, where these were 0.75*in.* x 0.75*in.* (19.1 *mm* x 19.1 *mm*)) in the plastic hinge zone (ranging from the top of footing to a distance equal to almost half of the height of walls above the top of footing) and for the rest of walls, 1*in.* (25.4 *mm*) wide by 2*in.* (80.8 *mm*) height (0.75*in.* x 1.5*in.* (19.1 *mm* x 38.2 *mm*) for Specimens T3 and T4) were used in order to reduce computation time of models. In both cases, the actual thickness of plates was used for the shell elements. The size of the elements was chosen based on previous nonlinear modeling study on composite walls by Polat and Bruneau [16] and to keep computational time within limits (for example, full hysteretic curves presented later took 8 to 10 days of computation time on the University at Buffalo Center for Computational Research's High-Performance Computers). For all steel plates, the Piecewise Linear Plasticity (*MAT_024* in LS-DYNA) material model was used with an Elastic Modulus (E) of 29000*ksi* (200,000 *GPa*), and Poisson's ratio of 0.3. The yield strengths obtained from coupon tests of steel plates were input into the material model; more specifically, these values were 55.4*ksi*, 55.2*ksi*, 54.0*ksi*, 54.0*ksi*, 61.03*ksi*, 60.03*ksi* (382 *MPa*, 381 *MPa*, 372 *MPa*, 372 *MPa*, 421 *MPa*, 414 *MPa*) for Specimens C1, C2, T1, T2, T3, and T4, respectively. The main reason for using this material model is because it provides the ability to input the complete effective stress versus effective plastic strain curves that were obtained from the coupon tests of the steel plates from each specimen. Fig. 4 shows the curves that were input into the material models of the specimens.

The plastic_kinematic (*MAT_003*) bilinear with kinematic hardening material model was used for the stiffener elements located at the base of the walls. The Elastic Modulus (*E*), Poisson's ratio, yield strength, Tangent Modulus (E_T), and Hardening parameter (β) were input as 29000*ksi* (200,000 *MPa*), 0.3, 50*ksi* (347 *MPa*), 290*ksi* (2000*MPa*), and 0.0 (i.e., bilinear elasto plastic material with 1 % strain hardening and

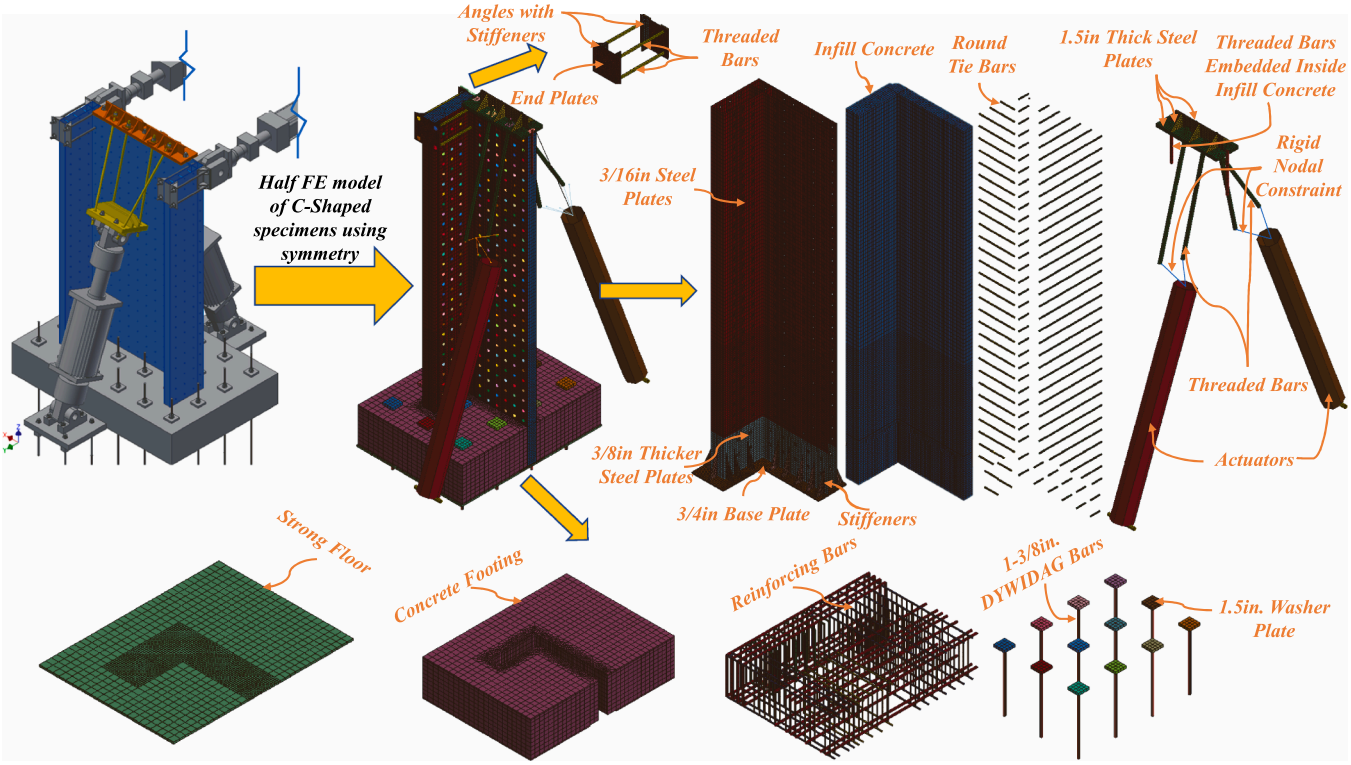

Fig. 1. Finite element model parts of a typical C-shaped wall specimen.

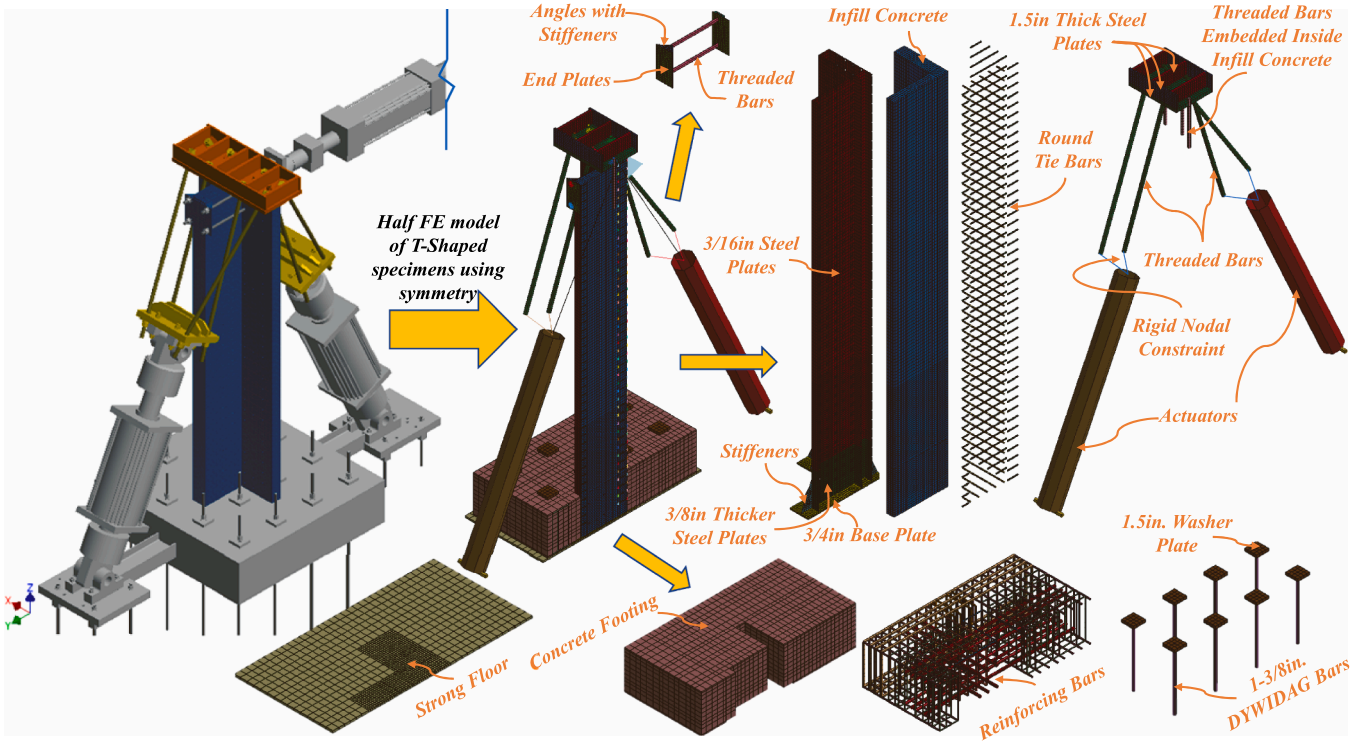

Fig. 2. Finite element model parts of a typical T-shaped wall specimen.

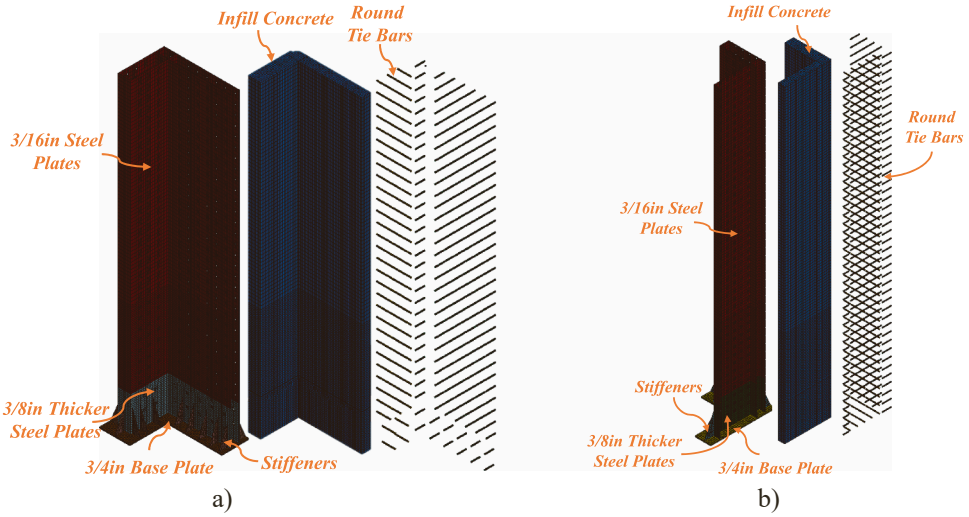

Fig. 3. Finite element model of a) C-, and; b) T-shaped wall specimens (1 in. = 25.4 mm).

zero isotropic hardening). Moreover, the shell elements of the stiffener plates were coupled with the solid elements of the base plates, and with the shell elements of thicker plates to simulate the fillet welds (i.e., mutual nodes were merged).

The Winfrith concrete material model (*MAT_085* in LS-DYNA) with eight-node constant stress solid elements (*Solid_1* in LS-DYNA) was used for the concrete parts (i.e., wall infill concrete and concrete of footing). The size of the solid elements in the walls plastic hinge zone (of same length as defined above) was 1 × 1 x 1 *in.* (25.4 *mm* x 25.4 *mm* x 25.4 *mm*) (0.75*in.* x 0.75*in.* x 1*in.* (19.1 *mm* x 19.1 *mm* x 25.4 *mm*) for Specimens T3 and T4). In the rest of the models, 1 × 2 x 1 *in.* (25.4 *mm* x 50.8 *mm* x 25.4 *mm*) (0.75*in.* x 1.5*in.* x 1*in.* (19.1 *mm* x 38.2 *mm* x 25.4 *mm*) for Specimens T3 and T4) solid elements were used to match the size of the steel elements. The parameters input in the material model are the elastic modulus (E_c), Poisson's ratio, concrete strength (f'_c), the tensile strength of concrete (f_t), fracture energy (FE), and aggregate size (ASIZE). The same Poisson's ratio of 0.2 and aggregate size of 0.5 were input in all models of specimens. The elastic modulus of concrete was calculated by using the equation in Section 19.2.2 of ACI 318–14 (Eq. 1 below).

Note that the Winfrith model does not account for the possible increase in concrete strength due to confinement by the steel plates around the infill concrete [17,18]. Hence, the compressive strength of the infill concrete was manually computed using equations by Susantha et al. [19] and the resulting values were input into the model to account for these effects. Modeling of the walls was also attempted using other concrete models, such as the KCC (Karagozian and Case Concrete) and CSCM (Continuous Surface Cap Model) concrete models [20], that can

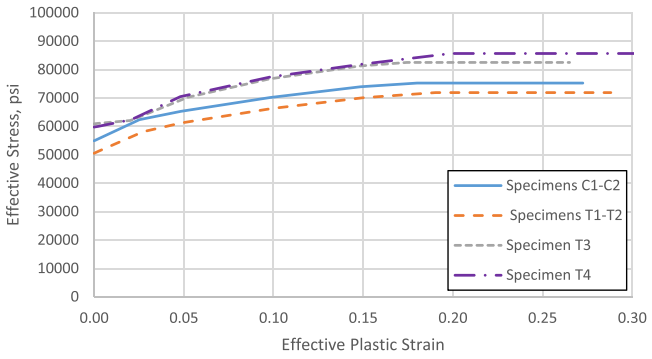

Fig. 4. Effective stress versus effective plastic strain curves used for MAT024 for specimens (1 ksi = 6.89 MPa).

account directly for this confinement effect, but it was still found that the Winfrith model with Susantha parameters better matched the test data (this will be shown with an example later), which is why this material model was retained in the end. The tensile strength of concrete (f_t) was taken as 10 % of the compressive strength of concrete (0.1 * f'_c). Finally, the fracture energy (FE) was given as the crack width at which crack normal tensile stress goes to zero, and it was calculated with Eq. 2 (note that for this, "*RATE*" in the material card needs to be set to 1).

$$E_c = 33 \; w_{conc}^{1.5} \sqrt{f'_c} \quad (in \;\; psi) \tag{1}$$

$$w_c = \frac{2G_f}{f_t} \tag{2}$$

where E_c is the elastic modulus, w_{conc} is the unit weight of concrete in lbf/ft^3, f'_c is the unconfined concrete strength in *psi*, w_c is the crack width at which crack normal tensile stress goes to zero, G_f is the area under the stress-crack opening relation (constant value of 0.514 was given for all specimens), f_t is the tensile strength of concrete (0.1 * f'_c).

The input values for infill concrete and footing's concrete in the Winfrith models for all of the specimens considered in this study are summarized in Table 2.

The post-peak behavior (crushing) of concrete cannot be modeled by the Winfrith material model. In other words, the model assumes constant stress after peak. Therefore, to model this, erosion of infill concrete elements (*MAT_ADD_EROSION_000* in LS-DYNA) were introduced into the models. No parametric study was performed to find the best parameter for the erosion here. Instead, the erosion criteria were taken from a similar study on steel plate concrete composite wall piers by Epackachi et al. [21]. They found out from their parametric study that minimum principal strain at failure of concrete should be − 0.04 for these types of walls. Therefore, the same parameter (*MNEPS* = - 0.04) was input to the erosion material card here.

The ties (and studs in Specimens T3 and T4) were modeled using two node beam elements with the Hughes-Liu beam formulation (*Beam_1* in LS-DYNA) and with two integration points (Gauss quadrature). The lengths of the beam elements matched with that of the solid elements of the infill concrete in order to merge the mutual nodes and create perfect bond between them. This was deemed acceptable as no slippage of tie bars was observed in the specimens during the tests. A plastic_kinematic material model with the Elastic Modulus (E) of 29000*ksi* (200,000 *MPa*), Poisson's ratio of 0.3, yield strength of 55*ksi* (379 *MPa*), Tangent Modulus (E_T) of 290*ksi* (2000*MPa*), and Hardening parameter (β) of 0.0 (zero isotropic hardening) was conservatively used for all tie bars and studs in all simulations. No fracture of tie bars was observed during tests (although tie bar welds eventually failed at wall drift deformation exceeding 3.57 %) and hence this is deemed acceptable. The fillet welds around the tie bars were modeled with *Rigid Nodal Constraints*. A hole having the same diameter as the tie bars was introduced in the steel plates and the end of beam elements and nodes around the holes were rigidly constrained. Note that the failure of welds around tie bars observed during testing of the specimens was not simulated in the models.

Base plates were modeled with a layer of eight-node constant stress solid elements (1 ×1 x 0.75*in.* (25.4 *mm* x 25.4 *mm* x 19.1 *mm*)). The plastic_kinematic material model was used with the Elastic Modulus (E) of 29000*ksi* (200,000 *MPa*), Poisson's ratio of 0.3, yield strength of 50*ksi* (345 *MPa*), Tangent Modulus (E_T) of 290*ksi* (2000*MPa*), and Hardening parameter (β) of 0.0. Moreover, the sizes of solid elements matched to the sizes of shell elements of thicker plates to merge the mutual nodes to simulate CJP weld.

3.1.1. Erosion of steel element of steel plates

The failure strain for eroding elements can also be specified in the *MAT_024* material model by defining an effective (or cumulative) plastic strain at failure. If such a failure strain is specified, the elements with *MAT_024* material model are eroded only after all the integration points in the element reach this failure strain. The cumulative plastic strain values (PS) at failure were obtained from the finite element analyses at the drifts when cracking was first experimentally observed. Table 3 shows an example calculation for the model of Specimen C1. The second and third columns in Table 3 are the drifts at which C-shaped wall specimens were displaced and the number of cycles applied to the walls at each cycle amplitude during the experiments, respectively. However, the LS-DYNA models were displaced with only one cycle at each cycle amplitude. The maximum effective plastic strain values obtained from LS-DYNA during cycles at various drifts, from an element between the 1st and 2nd tie bars that have the highest plastic strain, are shown in the fourth column of Table 3. Values are provided until the drift at which the fracture of steel plates of the specimen was observed during test. The maximum cumulative plastic strain that was extracted from this element was used to set-up the erosion criteria of the steel plates to replicate the fracture initiation at that drift (using *FAIL* in *MAT_024* model in LS-DYNA). The fifth column in Table 3 shows the plastic strain that the element gained in each individual cycle. These values were obtained by subtracting the cumulative strain in a given cycle from the cumulative strain in the previous cycle. Then, these values were multiplied by the number of cycles applied at each cycle amplitude in the third column of Table 3 in order to find the true cumulative plastic strain that developed in the specimen during the experiment, and these are shown in the sixth column of the table. The summation of the values in this sixth column is reported at the bottom of the table, which is 0.98 in this case. However,

Table 2
Concrete parameters for Winfrith concrete material model for infill concrete and footing (1 ksi = 6.89 MPa).

	Infill Concrete				Concrete in Footing			
Specimens	f'c, psi	Ec, ksi	ft, psi	FE	f'c, psi	Ec, ksi	ft, psi	FE
C1	5210	3695	520	0.00198	4700	3509	470	0.00219
C2	5900	3932	590	0.00174	5500	3796	550	0.00187
T1	3650	3093	365	0.00282	4410	3400	440	0.00234
T2	6520	4133	650	0.00158	5500	3796	550	0.00187
T3	6030	3975	600	0.00171	5550	3813	550	0.00187
T4	4900	3583	490	0.00210	5000	3620	500	0.00206

Table 3
Cumulative plastic strain calculation for the model of Specimen C1 (1 in. = 25.4 mm).

Cycle order	Drift, in.	Number of cycles for each drift, n	Cumulative plastic strain (PS) from LS-DYNA (single cycle)	PS_{i+1}-PS_i	n x PS_{i+1}-PS_i (corrected PS)
1	0.25/− 0.0125	2	0	0	0
2	0.5/− 0.25	2	0	0	0
3	0.75/− 0.375	2	0	0	0
4	1/− 0.5	2	0	0	0
5	1.38/− 1	2	0.0015	0.0015	0.00308
6	1.75/− 1.5	2	0.0094	0.0079	0.0158
7	2.63/− 2.25	3	0.072	0.063	0.188
8	3.5/− 3	3	0.24	0.17	0.504
9	5.25/− 4.5	3	**0.33**	0.09	0.27
10	7/− 6	2	*n.a.*	*n.a.*	*n.a.*
11	8.75/− 7.5	2	*n.a.*	*n.a.*	*n.a.*
12	10.5/− 9	4	*n.a.*	*n.a.*	*n.a.*
				Cumulative	**0.98**

these true cumulative plastic strain values were not used in the finite element analyses. Since walls were cycled with only one cycle per cycle amplitude in these analyses, the cumulative plastic strains directly from LS-DYNA were used in these models to trigger fracture; more specifically, these values were 0.33, 0.35, 0.5, 0.7 and 1.0 for Specimens C1, C2, T2, T3, and T4. At this time, it is unknown why different cumulative plastic strain values were obtained for each model. One could speculate that this was due to different tie bar spacings and bar sizes, different steel batch and fabrication details of specimens but a conservative value of 0.33 is suggested at this time. Note that fracture of the steel plates was not calculated for the model of Specimen T1 because, in this case, the fracture of the wall was due to the contribution of both elastic and plastic strains and a more detailed study would be needed to define a reliable value (because fatigue from elastic cycles is typically empirically determined for details that induce stress concentrations, on the basis of more extensive data than is available here).

3.1.2. Initial imperfection

Initial imperfections were generally not applied to the steel plates of the specimen models as their inelastic cyclic behavior was apparently sufficient to naturally create the out-of-straightness necessary to trigger local buckling, except for the models of Specimens T3 and T4 in which this buckling between the 1st and 2nd tie bar rows did not automatically occur as in the other models. Therefore, in these cases, an initial imperfection was applied to the nodes of steel plates and concrete elements right behind steel elements between the 1st and 2nd tie bar rows, with a sinusoidal shape of a maximum amplitude of 0.01125*in.* (0.286 *mm*) (=4.5*in.* (bar spacing)/400 (arbitrarily chosen)), and a wavelength of 9*in.* (228.6 *mm*) (2 times the tie bar spacing of 4.5*in.* (114.3 *mm*)).

3.2. Modelling of axial loading setup

The model of the Axial Loading Setup (ALS) (Fig. 5) consists of actuators, threaded bars, top plates, and stiffener plates.

The actuators were modeled with discrete beam elements (ELFORM=6) with area of 113in^3 (1.85E6mm^3), which is the same area of actuators in the laboratory. The Mat_Cable_Discrete_Beam (*MAT_071*) material model was chosen. Half of the force applied by the actuators (as half of the specimens were modeled) during the tests were input to this material model as an initial tensile force (*F0* in the material card) with 0.1 *sec* ramp-up time (*TRAMP* in the card) for the force and with 0.01 *sec* for the offset time (*TSTART*) at which the loading begins. The offset was arbitrarily selected as a time to tension the threaded bars of lateral loading setup (LLS) and to tension the DYWIDAG bars in the concrete footing (it will be explained later) before axial loading is applied to the wall to replicate the sequence of events during the test.

Threaded bars were modeled as two node beam elements (*Beam_1*)

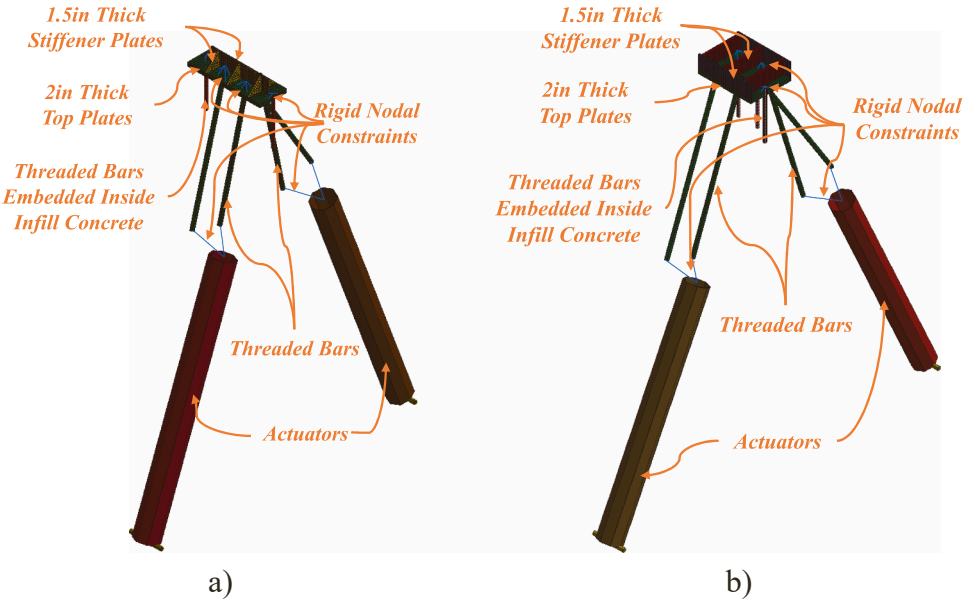

Fig. 5. Finite element model of axial loading setup for: a) C- and; b) T-shaped wall specimens (1 in. = 25.4 mm).

with the Hughes-Liu beam formulation and with two integration points (Gauss quadrature). The exact diameters of threaded bars were used in the beam formulations, namely 2*in.* (50.8 *mm*) for the ones connecting the top fixture and actuators, and 1.5*in* (38.1 *mm*) for the others embedded at the top of the wall. Again, these bars were modeled using a plastic_kinematic material model with the Elastic Modulus (E) of 29000*ksi* (200,000 *MPa*), Poisson's ratio of 0.3, yield strength of 105*ksi* (724 *MPa*), Tangent Modulus (E_T) of 0*ksi*, and Hardening parameter (β) of 0.0 (elastic perfectly plastic and zero isotropic hardening).

The top plate and stiffener plates were modeled with eight-node constant stress solid quadratic elements (smallest size being 1 ×1 x 0.5*in.* (25.4 ×25.4 ×12.7 *mm*)). The plastic_kinematic material model was again used in this case, with the Elastic Modulus (E) of 29000*ksi* (200,000 *MPa*), Poisson's ratio of 0.3, yield strength of 36*ksi* (248 *MPa*), Tangent Modulus (E_T) of 0*ksi*, and Hardening parameter (β) of 0.0 (elastic perfectly plastic and zero isotropic hardening). Moreover, the sizes of solid elements of both the top plate and stiffener plates matched at their connections to merge the mutual nodes and simulate fillet welds.

The fixtures that were attached to the actuators to connect the threaded bars, the seats for the threaded bars on top of the top plates, and the double spherical bolts were not included in the models used in the cyclic analysis. Instead, rigid nodal constraints were applied at the ends of the threaded bars to actuators and surface of top plate to provide the needed connectivity. The same method was used for the threaded bars embedded inside of the infill concrete to hold the axial load fixture on top of walls. This was deemed acceptable as no slippage or yielding of these plates were observed during testing of the specimens.

3.3. Modelling of lateral loading setup

The model of the Lateral Loading Setup (LLS) (Fig. 6) consists of end plates, angles with stiffeners and 1.5*in.* (38.1 *mm*) threaded bars.

Both end plates and angles with stiffeners were modeled with eight-node constant stress solid quadratic elements. The plastic_kinematic material model was used with the Elastic Modulus (E) of 29000*ksi* (200,000 *MPa*), Poisson's ratio of 0.3, yield strength of 36*ksi* (248 *MPa*), Tangent Modulus (E_T) of 0*ksi*, and Hardening parameter (β) of 0.0 (i.e., elasto-perfectly plastic with no strain hardening and no isotropic hardening).

Threaded bars were modeled the same way that the vertically inclined actuators were simulated. This is because, during bolting, and air-powered impact wrench was used to tighten the nuts, and this introduced 1000*lbf* (4.45*kN*) of force in the bars. Therefore, they were modeled with discrete beam elements (*ELFORM=6*) with an area of 1.405in^2 (23761mm^2), which is the area of the bars. The Mat_Cable_Discrete_Beam (*MAT_071*) material model was chosen. The 1000*lbf* (4.45*kN*) force was input to this material model as an initial tensile force (*F0* in the material card) with a 0.01 *sec* ramp-up time (*TRAMP* in the card) for the force.

The nuts were not modeled in the cyclic analysis. As was done for ALS, rigid nodal constraints were used between the ends of threaded bars and the nodes on the end plates where nuts were located (Fig. 6).

The lateral displacements were applied to walls at the pin of the actuators. The pin was modeled as a node and since the head of the actuators were bolted to LLS, the head of actuators were simulated as rigid nodal constraints, as shown in Fig. 7a. The walls were cycled at the node with the loading protocols specified for each test (Fig. 7b). The full cyclic analysis could not be run continuously beginning to end as this would have resulted in excessive computational time. However, from test observations, it was known that repetitive cycles at the same displacement amplitude resulted in the same magnitude of plastic strains. The cracks did not grow to be longer during the repetitive cycles. Therefore, in the finite element analyses, the walls were displaced with only one cycle at each cycle amplitudes of the loading protocol of the tests in order to decrease the computation time (Fig. 7b). Note that the restart property of LS-DYNA program was used, and four consequent analyses were performed to execute the full cyclic loading, which approximately took 10 days for each wall.

3.4. Modelling of reinforced concrete footing

The model of the reinforced concrete footing (Fig. 8) consists of the concrete of footing, reinforcing bars, DYWIDAG bars, and a part of the laboratory's strong floor.

The Winfrith concrete material model (*MAT_085*) with eight-node constant stress solid elements (*Solid_1*) was used for the concrete of the footing (as was done for the infill concrete of the walls). The size of solid elements ranged from 1 × 1 x 1 *in.* (25.4 ×25.4 ×25.4 *mm*) to 3.5 × 3.5 × 3.5 *in.* (88.9 ×88.9 ×88.9 *mm*), with the finer mesh surrounding the specimens and larger mesh away from the walls. The input values for the footing's concrete in the Winfrith models are shown in Table 2. The parameters were calculated the same way that those for the infill concrete were calculated. However, the unconfined compressive concrete strengths from cylinder tests were used for the concrete of footings.

Reinforcing bars (#4 for shear reinforcement, #6 for transverse reinforcement, and #9 and #10 for flexural reinforcement) were modeled as two node beam elements (*Beam_1*) with the Hughes-Liu beam formulation and with two integration points (Gauss quadrature). The exact diameters of each bar were used in the beam formulations. The plastic_kinematic material model was used with the Elastic Modulus (E) of 29000*ksi* (200,000 *MPa*), Poisson's ratio of 0.3, yield strength of 60*ksi* (414 *MPa*), Tangent Modulus (E_T) of 0*ksi*, and Hardening parameter (β) of 0.0. Also, the lengths of the reinforcing bars elements matched

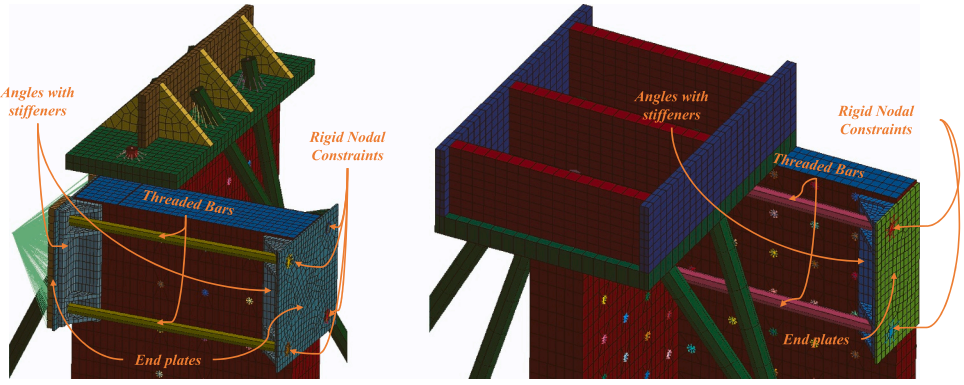

Fig. 6. Finite element model of lateral loading setup for: a) C- and; b) T-shaped wall specimens.

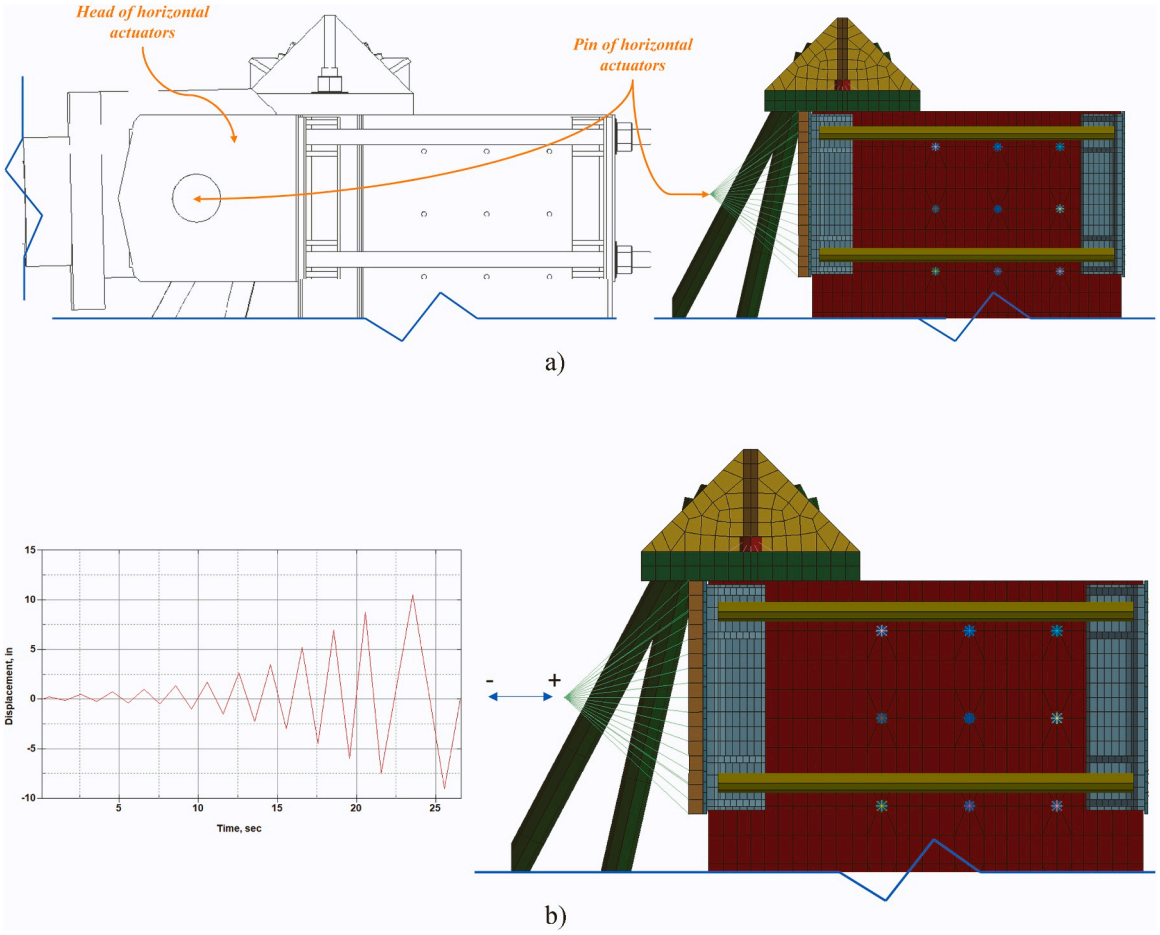

Fig. 7. Modeling at actuator pin: a) Schematic representation of the horizontal actuators and b) cyclic loading applied to walls.

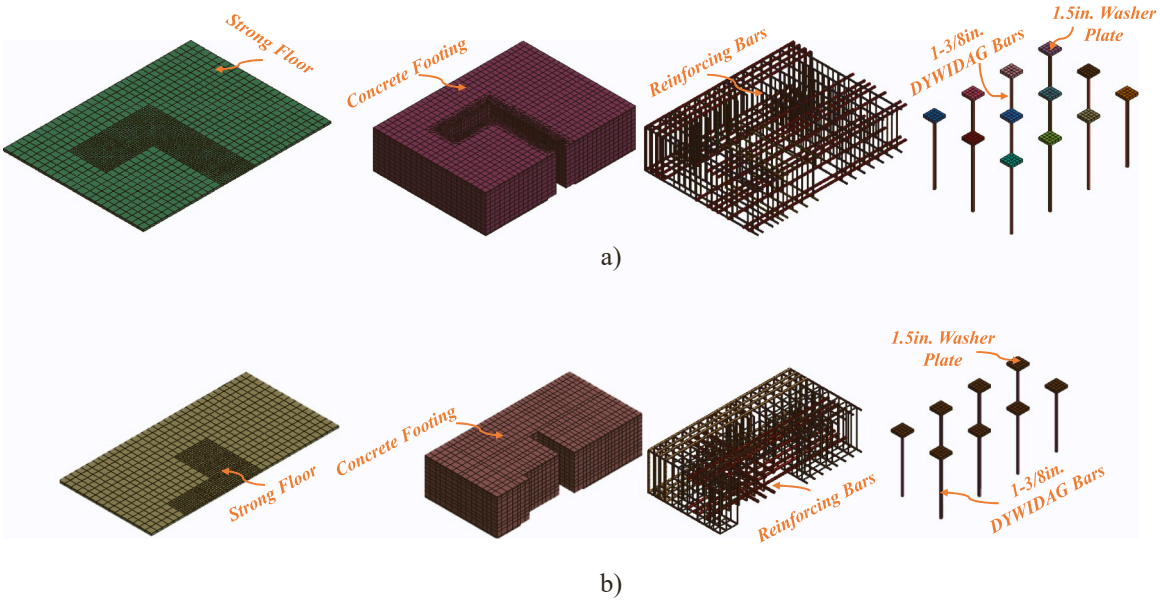

Fig. 8. Finite element model of reinforced concrete footing for: a) C- and; b) T-shaped wall specimens (1 in. = 25.4 mm).

the sizes of the solid elements in of concrete footing and the solid elements of the infill concrete (for the #10 reinforcing bars that go through the walls) to merge the mutual nodes and simulate the bonding between bars and concrete. Note that all the foundation rebars remained elastic. This is because the footings of specimens were designed to resist 1.2 time the plastic moment of the specimens.

The DYWIDAG bars were modelled with elastic material property (the Elastic Modulus (E) of 29000*ksi* (200,000 *MPa*)). Two node beam

elements (*Beam_1*) with the Hughes-Liu beam formulation and with two integration points (Gauss quadrature) was used for the element. Their post-tension was done by constantly pulling the ends of bars downward with a ramp-up curve having a 0.01 *sec* ramp-up time, until the end of cyclic loading. Load curve scale factor of − 0.126 and − 0.0606 for the models of C- and T- shaped walls, respectively, were given in the *Boundary _Prescribed_Motion_Set* card to have 130*kips* (578*kN*) of forces in the beam elements. These factors were found by trial and error. Note that negative values of the scale factors are to apply downward movement.

The strong floor and 1.5*in.* (38.1 *mm*) thick washer plates for the DYWIDAG bars were modelled with solid elements and rigid material model (*MAT_020*). Only the Elastic Modulus (*E*) was input; 3604*ksi* (24,849 *MPa*) for the strong floor (assuming 4*ksi* (27.6 *MPa*) concrete) and 29000*ksi* (200,000 *MPa*) for washer plates.

3.5. Boundary conditions

One boundary condition was applied to the models to restrict the movement of the base of the strong floor. Since it is modeled with rigid material model, only one node of an element under the strong floor was sufficient to restrain all translational and rotational directions. Another boundary condition was used to take advantage of symmetry and model only half of the walls. Note that buckling might be unsymmetric in the initial stage of buckling around the walls' perimeter. However, at end of the tests, the locations where buckling occurred was generally symmetric about the symmetry axis of the specimens. Moreover, the comparison between test data and numerical model results suggested that a small variation at the initial stage of buckling does not have a significant impact on global response. Therefore, only half of the walls' test setup was modeled in order to reduce computational time. Also, the ends of the beam elements for DYWIDAG bars were restrained in all directions except for the translational constraint in the z-direction so that they could be pulled down. Finally, the nodes for the base of actuators were restrained in all directions (i.e., fixed boundary condition).

3.6. Interface contacts

The interaction between steel plates and concrete as well as the interactions between foundation and strong floor, between base of infill concrete and top of base plate, and between bottom of top plate of ALS and top of infill concrete was defined with *automatic_surface_to_surface_mortar* contact model. This model is a segment-to-segment penalty-based contact and may provide more accurate results for contacts with higher order elements. Also, this model was recommended for implicit analysis [20]. This model is a penalty-based slave-node master-surface interaction where a force between slave-node and the master-surface is created by inserting a compression spring with a particular stiffness between the surfaces. In the models, a static interface friction coefficient of 0.3 was given, and the contact stiffness was increased as described below, (i.e., default value was not used). When [14] used the same contact model with the program default contact stiffness (SFS, SFM =1 in LSDYNA), slippage of the concrete core under large deformation occurred, and it was eliminated by increasing the contact stiffness of their wall models in the contact model definition. The contact stiffness was increased from the default, SFS = 1, by a factor of 3, 5 and 10. The model with the default contact stiffness (SFS = SFM = 1) showed a strength drop at 0.5 % drift during lateral deformation because of a sudden slippage of the concrete core, which was not observed in the tests of wall specimens tested by Alzeni and Bruneau [22]. Once the stiffness increased to SFS = SFM = 3 and 5, the sudden strength drop of the wall was delayed gradually to until 1.1 % and 1.6 % drifts, but not totally eliminated. The slippage of the concrete core, and therefore strength drop, was totally eliminated by having the contact stiffness equal to 10. Therefore, the contact stiffness of 10 (i.e., SFS = SFM = 10) was used here in order to avoid the same issue, i.e., slippage of the concrete core in the simulations. Note that contact surface model was needed because it was observed that even though steel elements buckled, the concrete elements were still carrying the load. In other words, it is critical to model the steel and concrete contact surface such that the steel and concrete elements can behave independently from the point when local buckling of the faceplate starts, up to fracture of the steel leading to specimen strength degradation. Slaving the steel and concrete modes at the interface would have prevented the steel faceplate from locally buckling, and would have led to erroneous analysis results because faceplate local buckling is an inherent and critically important part of the inelastic behavior of these composite walls.

LS-DYNA requires lots of memory when using the surface-to-surface contact model. Therefore, other but similar contacts were used for other parts of the models. The contacts between steel plates and concrete footing, between washer plates and concrete footing, between steel plates and top plate of ALS, and between base plate and concrete footing were done using *automatic_single_surface* model. It provides similar contact but is less computational expensive.

Lastly, the size of the solid elements for the angles with stiffeners in LLS could not be matched with the size of the steel plates and end plates, so this prevented the occurrence of mutual nodes that could be merged. Therefore, a *tie_nodes_to_surface_constrained_offset* model was used to tie the nodes of angles with stiffeners to the steel plates and end plates of LLS.

4. Results of finite element analysis

4.1. Initial finite element analysis

As mentioned before, three different concrete material models from LS-DYNA were tried to replicate the hysteretic behavior of the tested specimens, namely the Winfrith, KCC (Karagozian and Case Concrete), and CSCM (Continuous Surface Cap Model) material models [20]. The hysteretic results obtained with these models without erosions are shown in Fig. 9. Results from the Winfrith model matched well with the initial stiffness from test data in both positive and negative directions. Also, the maximum strength in the negative direction agreed well with test data but the results of FEA underestimated the maximum strength by 7.54 % in the positive direction. It is noteworthy that the pinching behavior of the hysteretic curves is well captured when using the Winfrith model. The model with KCC material model did not run for the complete hysteretic history. It run up to 1 % drift and could not satisfy the nonlinear equilibrium beyond that drift. Even though there are few results to compare with test data in this case, its partial results are still shown in Fig. 9. One noticeable observation from this analysis performed with the KCC model is that the stiffness obtained is 29 % higher

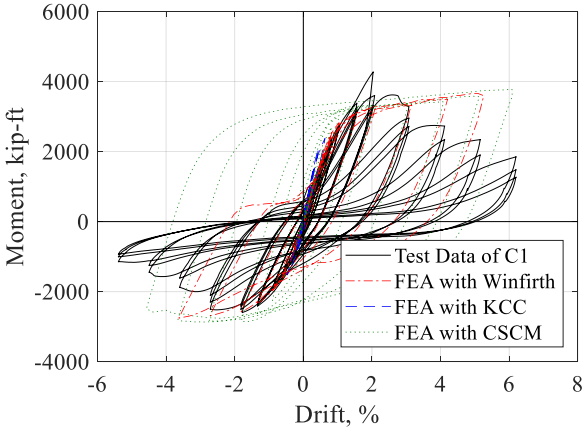

Fig. 9. Finite element results with different material model for concrete (1 ft = 304.8 mm; 1 kip = 4.45 kN).

than test data. The results with CSCM material model overestimated the strength in the negative direction by 9.46 % but almost matched the strength in the positive direction. However, as seen in Fig. 9, the model did not capture the pinching behavior of the hysteretic curves. The numerically obtained initial are 26 % higher.

Out of all concrete models considered, the Winfrith material model was chosen for further comparisons due to the good agreement with initial stiffness, pinching behavior, and good match with strength in the negative direction. The only issue with this material model was that the strength in the positive direction was underestimated by approximately 7.54 %. This was because this model does not include the effect of concrete confinement due to the presence of steel plates [17,18]. Therefore, to account for this effect, the concrete strengths obtained from compression tests and input into the model were increased to the value obtained using the equations from the study by Susantha et al. [19]. Results of FEA for concrete strength calculated with and without Susantha equations are shown in Fig. 10. Note that the erosion was not used in Fig. 10. With this approach (i.e., concrete strength corrected by the Susantha equation), the issue of having less strength in the positive direction was resolved and the FEA results matched better with test data. Therefore, the Winfrith model with Susantha parameters used for the infill concrete was used subsequently in the models of tested specimens.

4.2. Comparison between test data and finite element analyses

Comparisons between test data and the results of Finite Element Analysis (FEA) are useful as they provide, by calibration, an opportunity for the results of FEA to be used to help provide information that could not be measured from the specimens during tests. For this purpose, moment versus drift plots is used. The comparisons were done with respect to initial stiffness, maximum strength, and strength deterioration after peak. Figs. 11, 12, 13, 14, 15, and 16 show the comparison between test (left) and finite element analysis (right) of specimens for buckling on the web, buckling on the flange, and fracture on the web. Fig. 17a to 17f show the comparison between test data and the results of finite element analyses of tested specimens with (solid line) and without (dashed line) erosion on the left side of the figures. In assessing the adequacy of the model, comparison of results is only made between the test data and the results of the models with erosion (solid line). The results of FEA without erosion are also shown in the figures (dashed lines) but this is mainly because the models had to be run to determine the cumulative plastic strains to use in the erosion models. Numerical results without considering erosion also show that using an erosion model was needed to fully replicate the hysteretic curves better. Numerical results are also used to show the respective contributions of the concrete and steel parts of the specimens to the total flexural strength; these moments developed in both materials are drawn on the right side of Figs. 17a to 17f.

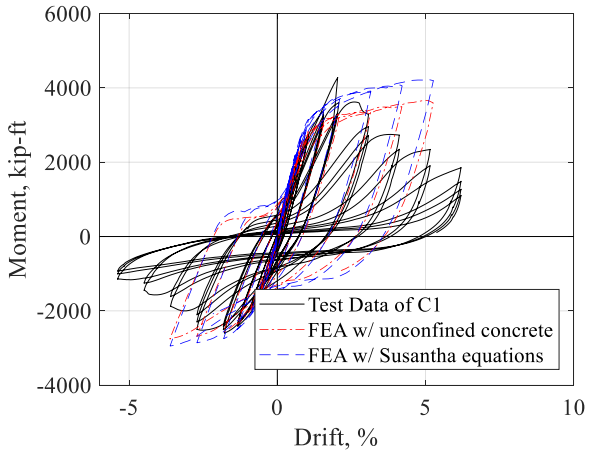

Fig. 10. Finite element results with and without Susantha parameters for concrete (1 ft = 304.8 mm; 1 kip = 4.45 kN).

Fig. 11 shows the comparison for the buckling in the web, the buckling in the flange and the fracture in the web between test and finite element model (FEM) of Specimen C1. The buckling in the web closure plate is 0.5*in.* (12.7 *mm*) higher in the FEM than observed in the experiment but buckling between tie bars matched with the observation during the test as well as the drifts (1.56 %) at which the buckling in the web occurred during the test of Specimen C1. The buckling in the flange also matched with test but it occurred at − 1.81 % in the test compared to − 2.71 % drift in the model. Finally, the total fracture length in the web at the end of test is 17*in.* (431.8 *mm*) in the model and is symmetric on both sides of the web, but it was 20*in.* (508 *mm*) long at the end of the test. Also, the initiation of fracture started at the CJP weld between the thicker steel plate in the foundation and the wall steel plates, and it propagated to connect to the fracture between tie bars, creating a non-symmetric path for the fracture, which cannot be captured by the model as the defect in CJP weld was not modelled. However, the model seems to capture the behavior well based on the results in Fig. 17a.

Fig. 17a shows the comparison between experimental and FEA results for Specimen C1. It is observed that the initial stiffnesses in the positive and in the negative directions are almost the same. Also, the maximum positive strength from FEA is 4.6 % higher than the experimentally obtained one for Specimen C1 (excluding the spurious peak of Specimen C1 in the positive direction, for reasons explained in Kenarangi et al. [1]) and maximum negative strengths are almost the same.

The strength degradation after maximum peak in the negative direction is close to the test data with a highest difference of 9.6 % between experimental and FEA results at − 3.6 % drift. However, the strength degradation in the positive direction did not match well and the largest difference observed between test data and FEA is 55.7 % at 5.2 % drift. The reason for this mismatch can be attributed to the rate of erosion of the concrete solid elements and the fact that an eroded element is completely removed from the model. Losing a 1 × 1 x 1*in.* solid element creates a gap in the models and causes a sudden drop of strength in the positive direction. In the positive direction, when the web is in compression, losing one such element implies losing 25 % of the web's width, whereas in the negative direction, when the flange is in compression, losing one such element implies losing 2.1 % of the flange's width, which explains the more sudden numerical drop in strength due to erosion when loading is applied in the positive direction. Note that using a finer mesh at the base of the wall models was tried in an attempt to get better results for the post peak behavior in the positive direction but even when using the super computers with largest memory and numbers of CPUs available from the CCR (Center for Computational Research) at the University at Buffalo, these finite element models (FEM) could not run because of insufficient memory. Therefore, at the time of this writing, this issue could not be resolved with the computational power available, and the same problem occurred in the FEM results for all walls.

The contribution of steel (dashed lines) and concrete parts (dotted lines) to total moment (solid lines) is shown in the right side of Fig. 17a. In the initial cycles, the steel contributes more to the total moment both in the positive and negative directions. As the wall reached its maximum strength (2.78 % drift), the steel plate buckled in the web at 1.56 % drift and concrete started to resist a greater percentage of the total strength. Therefore, the contribution from the concrete is slightly more than that of the steel at the maximum positive peak, more specifically 53.6 % for the concrete versus 46.4 % for the steel. However, as the wall started to lose its strength, this trend changed. The main contribution to the moment in the positive direction after 3.17 % drift until the end of test comes from steel. In contrast, the steel contributed 76.2 % of the total maximum moment at the maximum negative peak strength (−2.71 % drift). Also, in this case, once the steel plate buckled in the flange at − 2.71 % drift and the wall started to lose its strength, the main contribution to the moment in the negative direction remained from steel. Note that these contributions towards to the end of the cycles

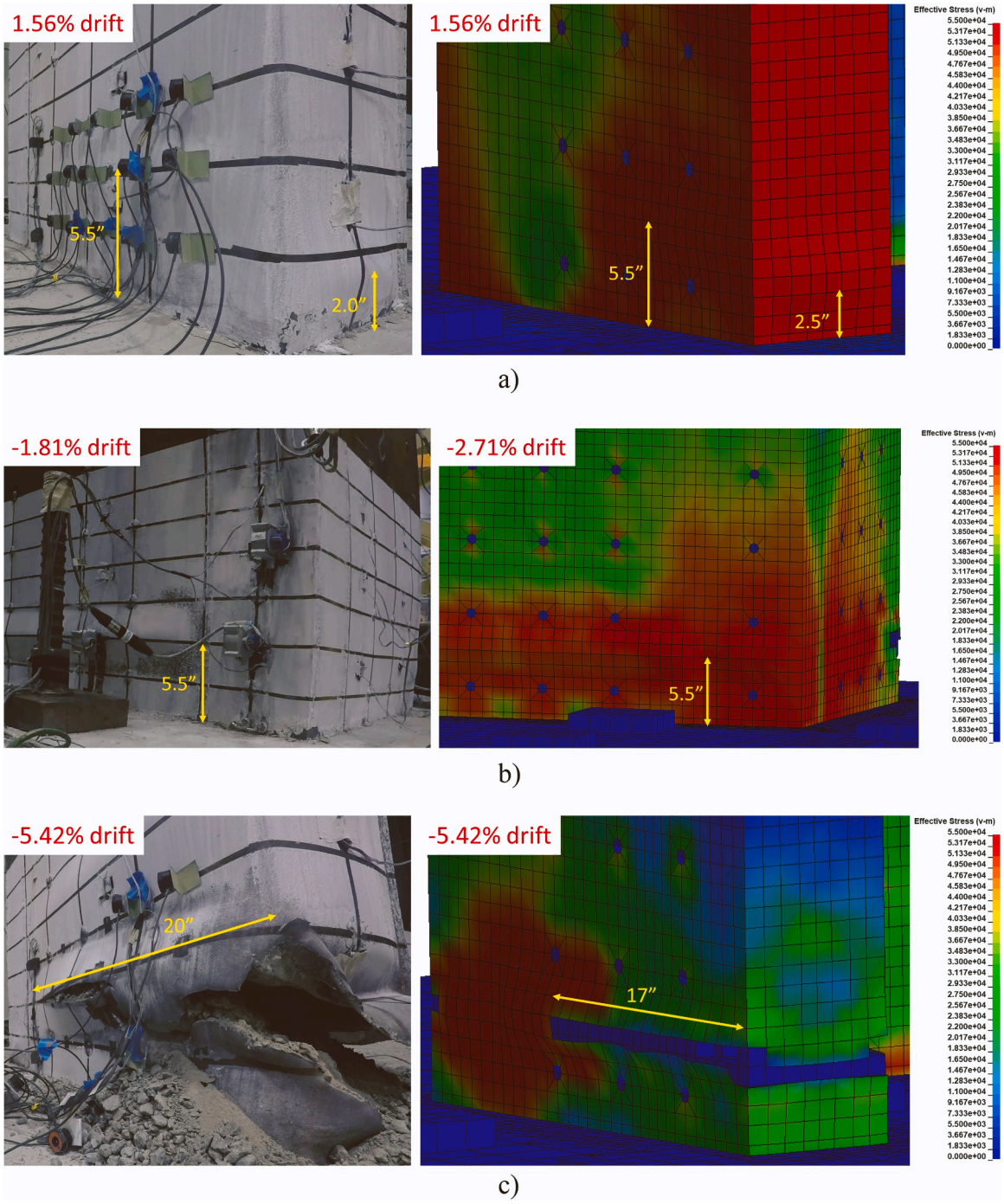

Fig. 11. The comparison between test (left) and finite element analysis (right) of Specimens C1 for: a) buckling in the web, b) buckling in the flange, and; c) fracture in the web.

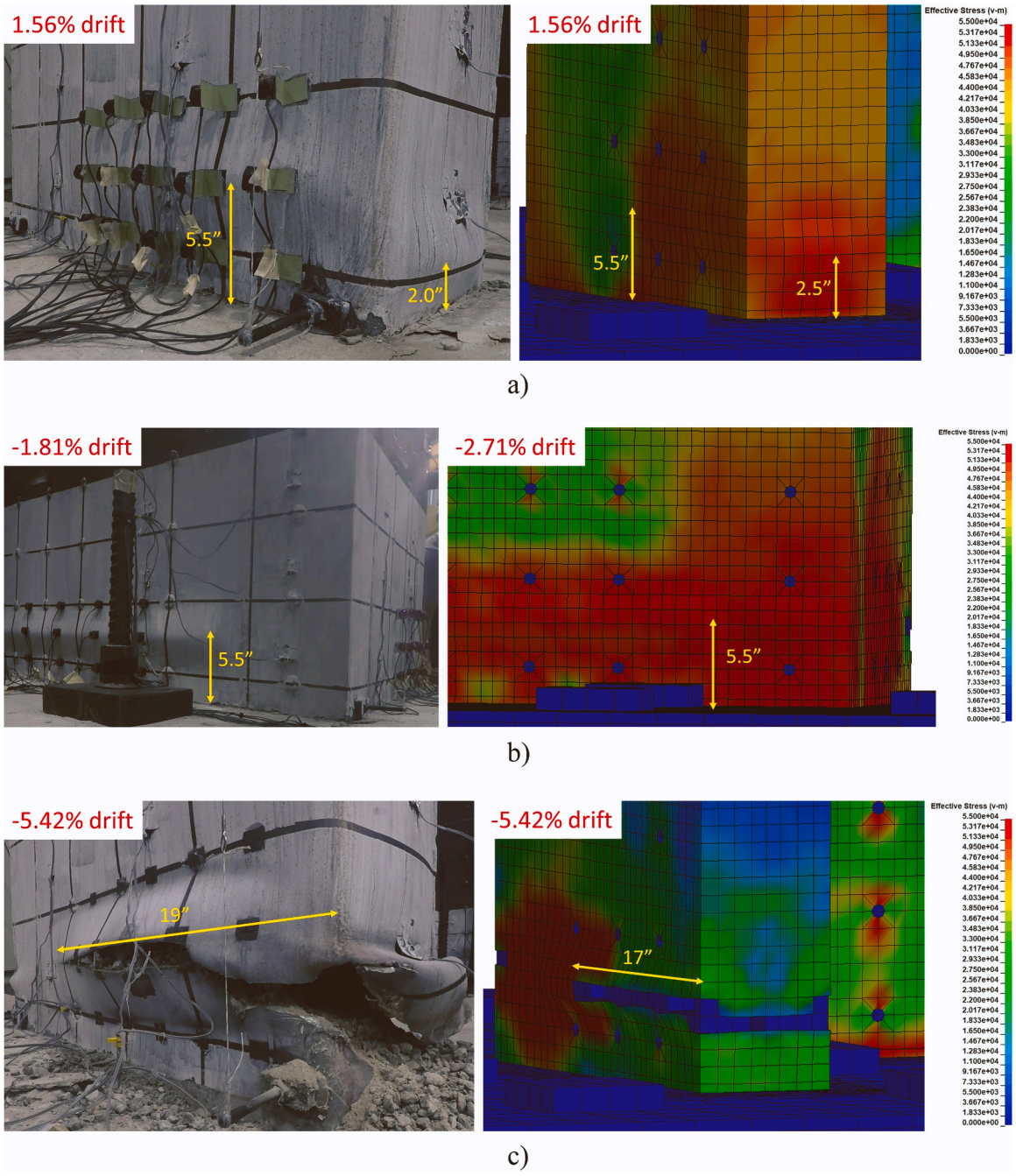

Fig. 12. The comparison between test (left) and finite element analysis (right) of Specimens C2 for: a) buckling in the web, b) buckling in the flange, and; c) fracture in the web.

history come from the unfractured part of the wall (i.e., from the flange). Moreover, the initial stiffness contribution from the steel does not change in both the positive and negative directions, but the initial stiffness contributed by the concrete in the positive direction is different than that in the negative direction. This is because the concrete elements only have strength in tension up to 0.1 f'_c (after which it drops to zero), and therefore, the moment of inertia contributed by the concrete in the negative direction is smaller than that in the positive direction, which causes the change of stiffness between the two directions.

Fig. 12 shows the comparison for the buckling in the web, the buckling in the flange and the fracture in the web between test and finite element model (FEM) of Specimen C2. The same behavior as for the model of Specimen C1 was observed in the model of Specimen C2 in terms of the locations of buckling and fracture, and drift at which these occurred.

Fig. 17b shows the comparison between experimental and FEA results for Specimen C2. The initial stiffnesses in the positive and the negative directions matched well, and they are almost the same. Also, the maximum positive and negative strengths obtained from the experiment and FEA are within 3.4 %/− 5.0 % of each other for Specimen C2 in the positive and negative directions, respectively. The strength degradations after maximum peak in the negative direction again agreed well with the test data with highest difference of 8.7 % between test data and FEA results at − 4.45 % drift. However, the strength degradation in the positive direction did not match well for the reason mentioned above and the largest difference observed between

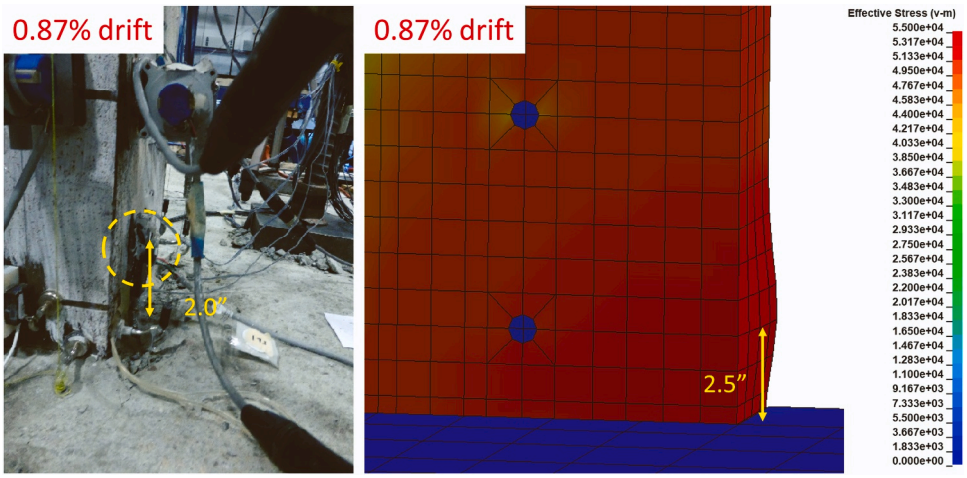

Fig. 13. The comparison between test (left) and finite element analysis (right) of Specimens T1 for buckling in the web.

the test data and FEA results is 47.2 % at 4.3 % drift. The right side of Fig. 17b shows the contribution of steel and concrete to total moment. The same trend as the FEA result of Specimen C1 is observed in the FEA results of Specimen C2 for the moment contribution from steel and concrete. Therefore, here only contribution from each material at maximum strength is reported. The contribution of concrete is 53.9 % versus 46.1 % for steel in the positive direction. On the other hand, steel contributed 77.0 % of the total maximum moment in the negative direction.

Fig. 13 shows the comparison for the buckling in the web between test and finite element model (FEM) of Specimen T1. The buckling in the web closure plate is 2.5*in.* (63.5 *mm*) from the top of the footing in FEM but it was at 2*in.* during test. However, both buckling occurred at the same drift (0.87 %).

Fig. 17c shows the comparison between experimental and FEA results for Specimen T1. The maximum positive and negative strengths obtained from the experiment and FEA are within 12.3 %/− 11.2 % of each other for Specimen T1. The initial stiffnesses in the positive and the negative directions matched well, and they are almost the same. The right side of Fig. 17c shows the contributions to the total moment from both steel and concrete. It is clear that in the initial cycles, the steel contributes more to the total moment both in the positive and the negative directions. The contributions from steel to the total maximum moments are 62.3 % at 0.87 % drift and 79.0 % at − 0.87 % drift in the positive and the negative directions, respectively.

Fig. 14 shows the comparison for the buckling in the web, the buckling in the flange and the fracture in the web between test and finite element model (FEM) of Specimen T2. The buckling in the web closure plate is 2.5*in.* (63.5 *mm*) in FEM from the top of the footing but it was at 2*in.* (50.8 *mm*) during test. Buckling between tie bars matched with the observation during the test and buckling occurred at the same drift (1.36 %). The buckling in the flange happened at − 2.48 % drift in the model but it occurred at − 1.66 % drift in the test. Finally, the total fracture length in the web is 11*in.* in the model but it was 18*in.* at the end of the test, but in this case too, fracture initiated at CJP weld between the thicker steel plate in the foundation and the wall steel plates. This cannot be captured by the model as the defect in CJP weld was not modeled. However, the model seems to capture the behavior with combination of the erosion of steel and concrete together based on the results in Fig. 17d.

Fig. 17d shows the comparison between experimental and FEA results for Specimen T2. In this case, the FEA models underestimated the maximum positive and negative strengths by 7.2 %/− 10.1 %, respectively, compared to the experimental values. The initial stiffness from FEA in the positive direction is 30 % higher than observed experimentally but the initial stiffness in the negative direction matched well. The strength degradation after maximum peak in negative direction are close to the test data with highest difference of 8.7 % between test data and FEA results at − 2.5 % drift. However, the strength degradation in the positive direction did not match well and the largest difference observed between test data and FEA results is 70.3 % at 4.4 % drift.

The contribution of steel (dashed lines) and concrete parts (dotted lines) to total moment (solid lines) is shown in the right side of Fig. 17d. Different from the FEA of C-shaped walls, in the initial cycles, the steel and concrete contributes almost equally to the total moment in the positive direction, but steel contributes more to the negative direction. As the wall reached 1.36 % drift, the steel plate buckled in the web and then concrete started to resist a greater percentage of the total strength. Therefore, the contribution from the concrete is slightly more than that of the steel at the maximum positive peak, more specifically 59.1 % for the concrete versus 40.9 % for the steel. However, as the wall started to lose its strength, this trend changed. The main contribution to the moment in the positive direction after 2.81 % drift until the end of test comes from steel. In contrast, the steel contributed 65.8 % of the total maximum moment at the maximum negative peak (−1.62 % drift). Also, in this case, once the steel plate buckled in the flange at − 2.43 % drift and the wall started to lose its strength, the main contribution to the moment in the negative direction remained from steel.

Fig. 15 shows the comparison for the buckling in the web, the buckling in the flange and the fracture in the web between test and finite element model (FEM) of Specimen T3. Since studs were added to the specimen and an initial imperfection was applied to the model of Specimen T3, the buckling in the web closure plate, and between tie bars in the web and the flange occurred at the same height as the observation from the test. Buckling in the web occurred at 1.36 % drift but buckling in the flange occurred at − 1.66 % in the test but it occurred at − 2.48 % drift in the model. However, a complete analysis covering all of the hysteresis loops could not be run in this case and the fracture in the corner was the only part of the failure replicated by the model before it stopped running.

Fig. 17e shows the comparison between experimental and FEA results for Specimen T3. The FEA models underestimated the maximum positive and negative strengths by 10.5 %/− 7.4 %, respectively, compared to the experimental values. The initial stiffness from FEA in the positive direction is 16.7 % less than observed experimentally but the initial stiffness in the negative direction matched well. The strength

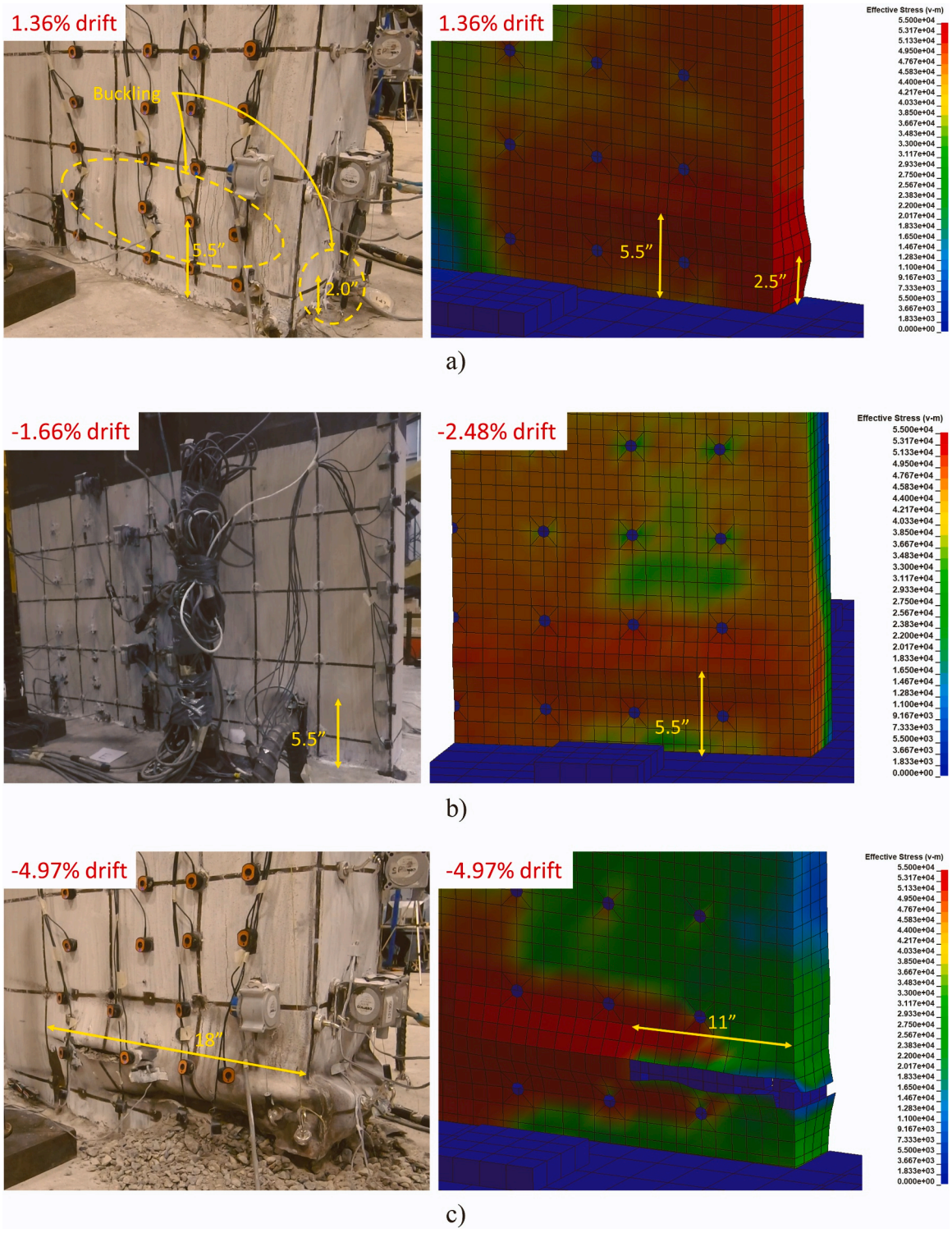

Fig. 14. The comparison between test (left) and finite element analysis (right) of Specimens T2 for: a) buckling in the web, b) buckling in the flange, and; c) fracture in the web.

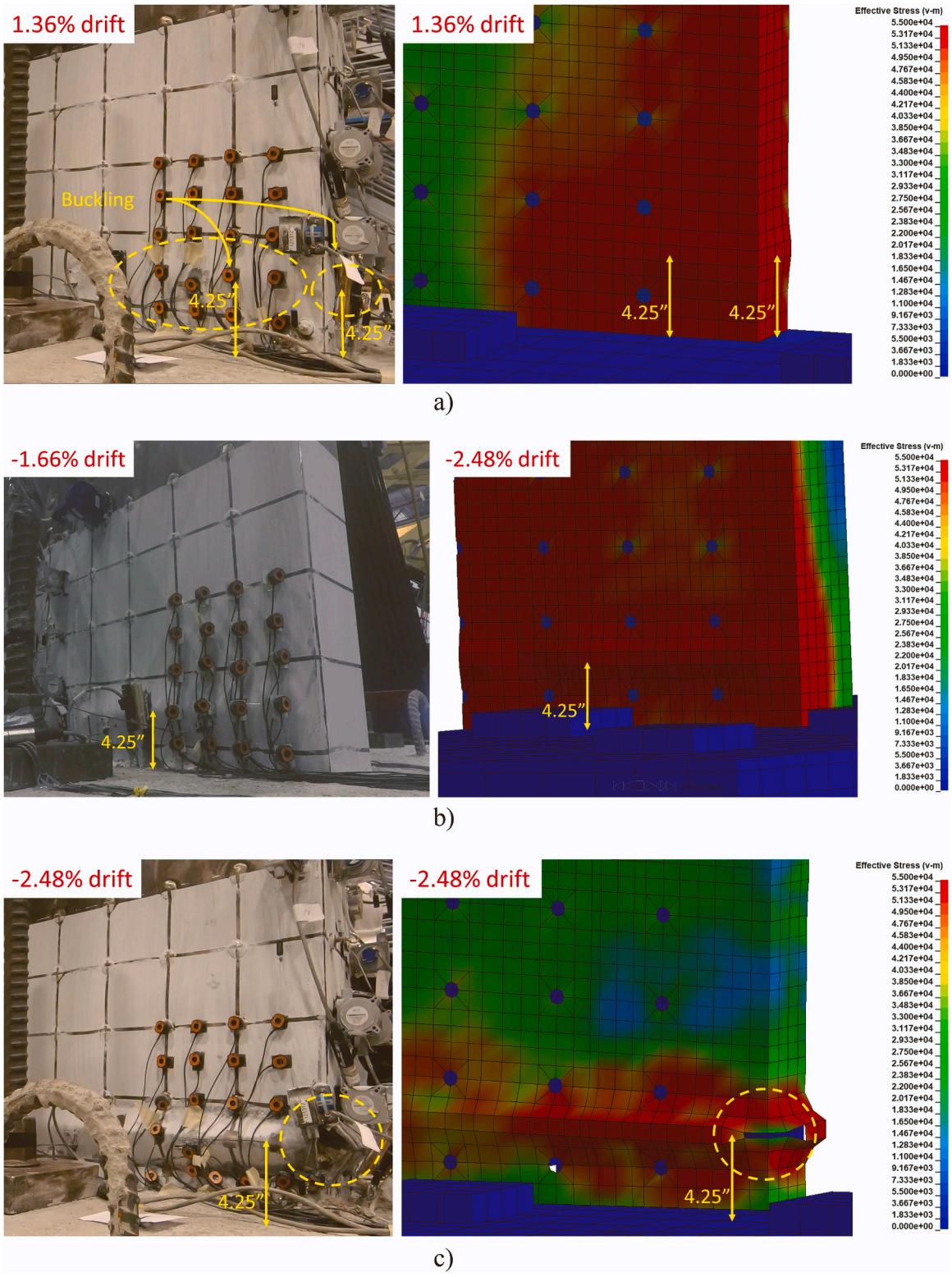

Fig. 15. The comparison between test (left) and finite element analysis (right) of Specimens T3 for: a) buckling in the web, b) buckling in the flange, and; c) fracture in the web.

degradations after maximum peak could not be obtained for this specimen. The right side of Fig. 17e shows the contributions to the total moment from both steel and concrete. The same trend as the FEA result of Specimen T2 is observed in the FEA results of Specimen T3 for the moment contributions from steel and concrete. Therefore, here only the contribution from each material at maximum strength is reported. The contribution of concrete is 56.6 % versus 43.4 % for steel in the positive direction. On the other hand, steel contributed 62.3 % to the total maximum moment in the negative direction.

Fig. 16 shows the comparison for the buckling in the web, the buckling in the flange and the fracture in the web between test and finite element model (FEM) of Specimen T4. Like the model of Specimen T3, the buckling in the web closure plate, and the buckling between tie bars in the web and the flange occurred at the same height as the observation from the test. The location of the fracture initiation is also the same. However, the sudden fracture in the web could not be replicated. The

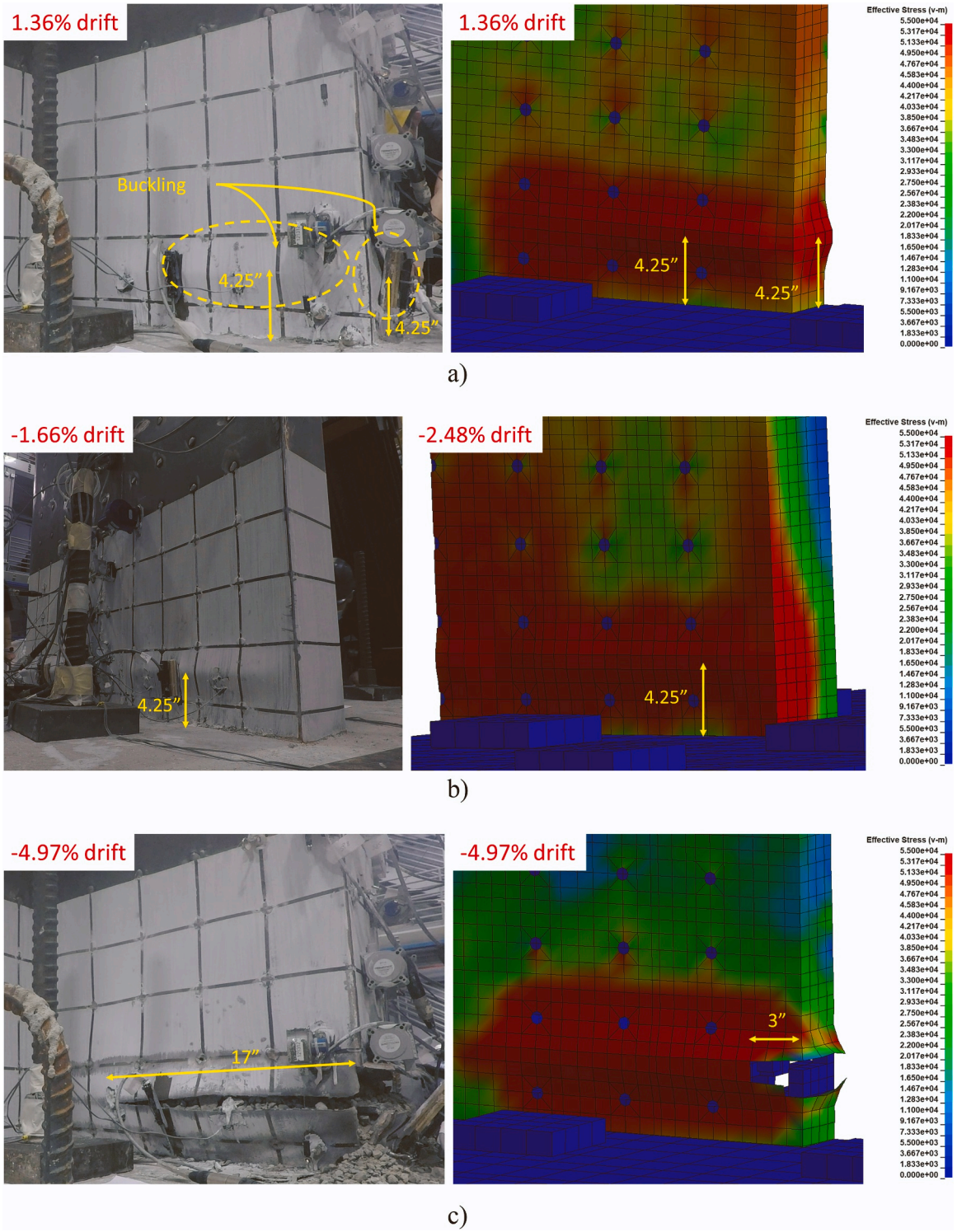

Fig. 16. The comparison between test (left) and finite element analysis (right) of Specimens T4 for: a) buckling in the web, b) buckling in the flange, and; c) fracture in the web.

total fracture in the web is 3*in.* (76.2 *mm*) in the model but it was 17*in.* (432 *mm*) at the end of the test. Therefore, the results from the FEA in Fig. 17f did not match with the experimental results as well as for the other specimens.

Fig. 17f shows the comparison between experimental and FEM results for Specimen T4. The FEA models underestimated the maximum positive and negative strengths by 14.1 %/− 10.0 %, respectively. The initial stiffness both in the positive and the negative directions matched

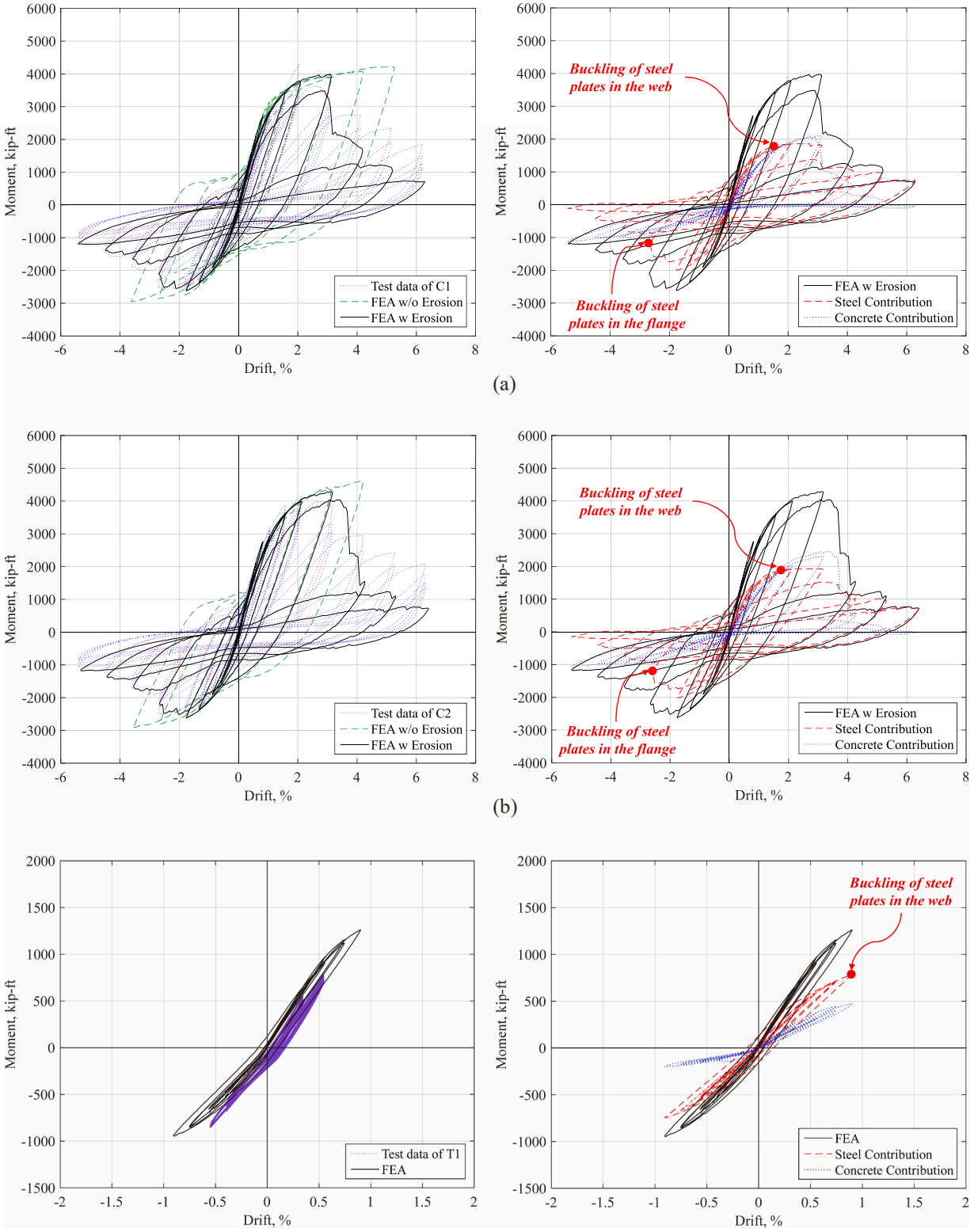

Fig. 17. The comparison between test results (left) and the contribution to moment from steel and concrete parts (right) for Specimens a) C1, b) C2, c) T1, d) T2, e) T3, and; f) T4 (1 ft. = 304.8 mm; 1 kip = 4.45 kN).

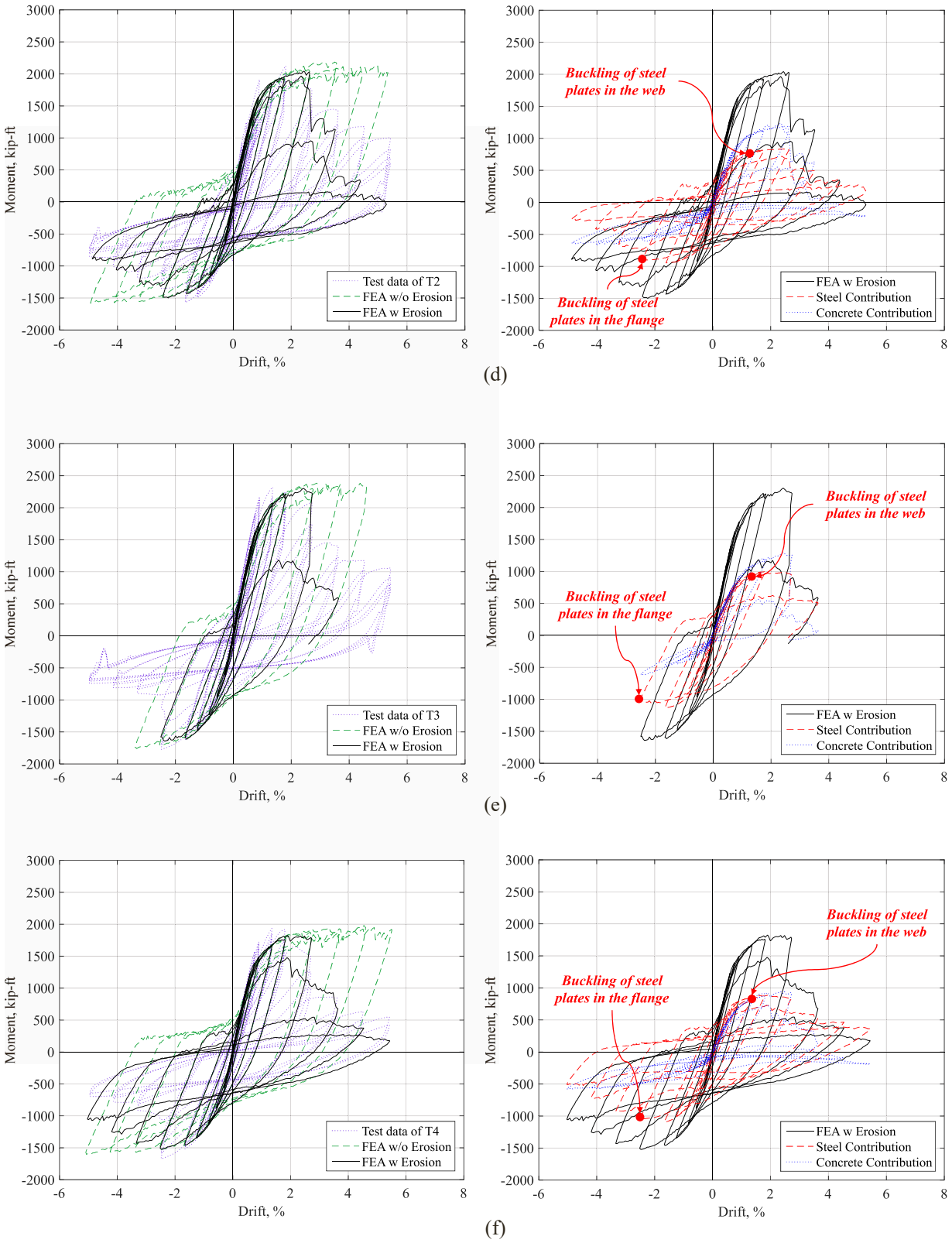

Fig. 17. (*continued*).

well. The strength degradations after maximum peak both in the positive and the negative directions did not match, and the largest differences observed between the test data and FEA is 67.8 % at 5.42 % drift and 59.0 % at − 3.3 %. The right side of Fig. 17f shows the contributions of steel and concrete to total moment. The same trend as the FEA results of Specimens T2 and T3 is observed in the FEA results of Specimen T4 for the moment contributions from steel and concrete. Therefore, here only contribution from each material at maximum strength is stated. The contribution of concrete is 50.7 % versus 49.3 % for steel in the positive direction. On the other hand, steel contributed 69.3 % to the total

Table 4
Summary of findings in Fig. 17.

Specimens	$Moment_{FEA}/Moment_{Test}$ (At Peak)		Maximum $Moment_{FEA}/Moment_{Test}$ (After Peak)		Contribution to Total Moment Strength At Peak (Steel / Concrete)	
	(+) Drift	(-) Drift	(+) Drift	(-) Drift	(+) Drift	(-) Drift
C1	104.6 %	100.0 %	44.3 %	109.6 %	46.4 % / 53.6 %	76.2 % / 23.8 %
C2	103.4 %	105.0 %	52.8 %	108.7 %	46.1 % / 53.9 %	77.0 % / 23.0 %
T1	112.3 %	111.2 %	n.a.	n.a.	62.3 % / 37.7 %	79 % / 21 %
T2	92.8 %	89.0 %	29.7 %	108.7 %	40.9 % / 59.1 %	65.8 % / 34.2 %
T3	89.5 %	92.6 %	n.a.	n.a.	43.4 % / 56.6 %	62.3 % / 37.7 %
T4	85.9 %	90.0 %	32.2 %	41.0 %	49.3 % / 50.7 %	69.3 % / 30.7 %

maximum moment in the negative direction.

The findings in Fig. 17 are summarized in Table 4.

5. Summary and conclusions

The material presented above described the details of the finite element models of the tested specimens and showed the comparison between experimental results for the tested specimens and the numerical results from the finite element analyses (FEA) of these specimens. Detailed 3D modeling was preferred to replicate the test results because of its ability to more accurately capture the nonlinear inelastic response of the walls during cyclic loading and the significant shifts in neutral axis position during loading reversals due to the specific cross-section shape of the walls. Moreover, the numerical models provided here were verified to be appropriate for walls having the more complex C- and T-shaped cross-sections walls (whereas previous work by [13,23], and others focused on planar walls without and with axial loads. Simpler modeling approaches for these walls to be used by practicing engineers in OpenSees analyses have been provided in another paper [16]. Moment versus drift plots were used for this purpose, and the initial stiffness, maximum strength, and strength deterioration after peak were compared.

The FEA results matched well with the experimental results of all specimens with respect to strength, initial stiffness, and maximum strength, with differences of no more than 30 % for initial stiffness and 14.1 % for the maximum strength. With respect to strength degradation, degradation in the negative direction (i.e., putting the flange in compression) was reasonably well captured by the use of eroding steel and concrete elements, with maximum differences of 9.6 % at large drifts of − 3.6 % in the results of Specimen C1, except for Specimen T4 where this difference became as large as 67.8 % at 5.4 % drift. However, the strength degradation in the positive directions (i.e., putting the web in compression) was not matched as well by the numerical results, with differences of up to 70.3 % at large drifts of 4.4 % in the result of Specimen T2. The reason of this mismatch is because the erosion of a concrete solid element, which creates a gap in the model and causes a sudden drop of strength, has a more significant impact for loading in the positive direction since there are fewer concrete elements in compression across the web than across the flange. Using a finer mesh at the base of wall models was attempted to reduce the error in the positive direction during element erosion, but these finite element models (FEM) did not run because of insufficient computer memory (even the shared percentage of the University super computer that could be allocated to a single user (12 processors out of 200,000 available cores and 1000 M memory) by the Center for Computational Research at the University at Buffalo). Therefore, this issue could not be further investigated due to limitations in the computational power available.

The respective contributions of steel and concrete to the total flexural strength was also investigated with the help of FEA. It was found out that in the initial cycles of hysteretic response for the C-shaped specimens, the steel contributed more to the total flexural strength, both in the positive and negative directions (on average 54 % and 80 % in each of these directions, respectively). The contribution of steel and concrete in the T-shaped specimens were almost the same in the initial cycles in the positive direction, but steel contributed more to the negative direction as was the case for the C-shaped specimens (on average 51 % and 68 % in each of these directions, respectively).

Then, for both the C- and T-shaped specimens, as the walls reached their maximum strength in the positive directions, the steel plates buckled in the web and concrete progressively started to provide a greater percentage of the flexural strength; as a result, concrete contributed more than steel at the maximum positive peak (on average 55 % for concrete versus 45 % for steel). However, as the wall started to undergo strength degradation, the main contribution to flexural strength in the positive direction returned to be from steel again (on average 20 % for concrete versus 80 % for steel).

In contrast, in the negative direction, the steel contributed more to the total maximum moment (on average 30 % for concrete versus 70 % for steel). However, once the steel plate buckled in the flange and the wall started to lose its strength, the main contribution to the moment in the negative direction became from concrete (on average 74 % for concrete versus 26 % for steel).

Moreover, the initial stiffness contribution from the steel did not change in both the positive and negative directions (as expected), but the contribution to initial stiffness from concrete in the positive direction was different than that in the negative direction. This is again expected, since the concrete elements do not have a significant strength in tension, but the numerical results above have allowed to compare these respective contributions and illustrate why the wall stiffness changed between the two loading directions.

It is foreseen that the validated model presented here can be useful in future studies, including research to investigate the sensitivity of cumulative strain predictions on ultimate behavior, in parallel with low-cycle fatigue studies to establish more robust limiting cumulative strain parameters.

CRediT authorship contribution statement

Emre Kizilarslan: Writing – original draft, Visualization, Software, Resources, Methodology, Formal analysis, Data curation, Conceptualization. **Hadi Kenarangi:** Writing – review & editing, Supervision, Software, Formal analysis, Conceptualization. **Michel Bruneau:** Writing – review & editing, Writing – original draft, Supervision, Resources, Project administration, Methodology, Funding acquisition, Conceptualization.

Declaration of Competing Interest

The authors declare that they have no known competing financial interests or personal relationships that could have appeared to influence the work reported in this paper.

Acknowledgements

This research was performed with support from the CharlesPankow Foundation (CPF) and the American Institute of Steel Construction (AISC), through CPF research Grant #06-16 awarded to co-PIs Michel Bruneau, from University at Buffalo and Amit H.Varma, from Purdue University. This paper focuses on a part of thework conducted at the University at Buffalo only. The researchers also thank Magnusson Klemencic Associates (MKA), Cives Steel Co., J. F. Stearns Co., and Turner Construction, for donating steel and fabrication of specimens tested. The authors also thank members of the Project Advisory Team (Ron Klemencic, Chairman and CEO, MKA; Larry Kruth, Vice President, American Institute of Steel Construction (AISC); Jim Malley, Senior Principal, Degenkolb Engineers; Ron Hamburger, Senior Principal at SGH; Devin Huber, Director of Research, AISC) for their valuable technical guidance. All opinions, findings, conclusions, and recommendations presented in this paper are those of the authors and do not necessarily reflect the view of the sponsors.

References

[1] Dan D, Fabian A, Stoian V. Theoretical and experimental study on composite steel-concrete shear walls with vertical steel encased profiles. J Constr Steel Res 2011; 67:800–13.
[2] Rahai A, Hatami F. Evaluation of composite shear wall behavior under cyclic loadings. J Constr Steel Res 2009;65:1528–37.
[3] Zhao, Q., Astaneh-Asl, A. (2004) Cyclic behavior of traditional and innovative composite shear walls, 13th World Conference on Earthquake Engineering, Vancouver, Canada, 13 WCEE, August 2004.
[4] Zhao Q, Astaneh-Asl A. Seismic behavior of composite shear wall systems and application of smart structures technology. Steel Struct 2007;7:69–75.
[5] Zhao Q, Astaneh-Asl A. Cyclic behavior of traditional and innovative composite shear walls. J Struct Eng 2004;130(2):271–84.
[6] Rahnavard R, Hassanipour A, Mounesi A. Numerical study on important parameters of composite steel-concrete shear walls. J Constr Steel Res 2016;121: 441–56.
[7] Wright D, Oduyemi TOS, Evans HR. The design of double skin composite elements. , J Constr Steel Res 1991;19:111–32.
[8] McKinley B, Baswell LF. Behaviour of double skin composite construction. , J Constr Steel Res 2002;58:1347–59.
[9] Wright HD, Gallocher SC. The behaviour of composite walling under construction and service loading. , J Constr Steel Res 1995;35:257–73.
[10] Omer, A.A., Mohamedien, A.R., Agour, A.A., Yones, M.M. (2009) Modeling and analysis of double skin composite plates, 13th International Conference on AEROSPACE SCIENCES & AVIATION TECHNOLOGY, Cairo, Egypt, ASAT-13, May2009.
[11] Kizilarslan E, Broberg M, Shafaei S, Varma AH, Bruneau M. Non-linear analysis models for composite plate shear walls-concrete filled (C-PSW/CF). J Constr Steel Res 2021;Vol 184. https://doi.org/10.1016/j.jcsr.2021.106803.
[12] Shafaei S, Varma AH, Broberg M, Klemencic R. Modeling the cyclic behavior of composite plate shear walls/concrete filled (C-PSW/CF). J Constr Steel Res 2021; 184:106810.
[13] Kenarangi H, Kizilarslan E, Bruneau M. Cyclic behavior of c-shaped composite plate shear walls–Concrete filled. Eng Struct 2020;226:111306.
[14] Kizilarslan E, Bruneau M. Cyclic behavior of T-shaped composite plate shear walls–concrete filled. J Struct Eng 2023;149(8):04023102.
[15] Hallquist JO. LS-DYNA keyword user's manual. Livermore Softw Technol Corp 2007;970:299–800.
[16] Polat E, Bruneau M. Modeling cyclic inelastic in-plane flexural behavior of concrete filled sandwich steel panel walls. Eng Struct 2017;148:63–80.
[17] Coleman, D.K. (2016). Evaluation of concrete modeling in LS-DYNA for seismic application." PhD diss., 2016.
[18] Wu, Y., Crawford, J.E., and Magallanes, J.M. (2012) Performance of LS-DYNA concrete constitutive models. Proc., 12th International LS-DYNA users conference, 1–14.
[19] Susantha K, Ge H, Usami T. Uniaxial stress–strain relationship of concrete confined by various shaped steel tubes. Eng Struct 2001;23(10):1331–47.
[20] Hallquist JO. LS-DYNA theory manual. Livermore Softw Technol Corp 2006;3: 25–31.
[21] Epackachi S, Whittaker AS, Varma AH, Kurt EG. Finite element modeling of steel plate concrete composite wall piers. Eng Struct 2015;100:369–84.
[22] Alzeni Y, Bruneau M. In-plane cyclic testing of concrete-filled sandwich steel panel walls with and without boundary elements. J Struct Eng 2017;143(9):04017115.
[23] Polat E, Bruneau M. Cyclic inelastic in-plane flexural behavior of concrete-filled, sandwich steel panel walls with different cross-section properties. Eng J, Am Inst Steel Constr 2018;55:45–76.